Atmospheric
Chemistry
and Physics

Lower-tropospheric CO₂ from near-infrared ACOS-GOSAT observations

Susan S. Kulawik[1], Chris O'Dell[2], Vivienne H. Payne[3], Le Kuai[4], Helen M. Worden[5], Sebastien C. Biraud[6], Colm Sweeney[7], Britton Stephens[7], Laura T. Iraci[8], Emma L. Yates[1], and Tomoaki Tanaka[8]

[1]Bay Area Environmental Research Institute, Sonoma, CA, USA
[2]Cooperative Institute for Research in the Atmosphere, Colorado State University, Fort Collins, CO, USA
[3]Jet Propulsion Laboratory, California Institute of Technology, Pasadena, CA, USA
[4]UCLA Joint Institute for Regional Earth System Science and Engineering (JIFRESSE), Los Angeles, CA, USA
[5]Atmospheric Chemistry Observations & Modeling (ACOM) Laboratory, National Center for Atmospheric Research, Boulder, CO 80307 USA
[6]Lawrence Berkeley National Laboratory, Earth Science Division, Berkeley, CA, USA
[7]NOAA/ESRL/GMD, Boulder, CO, USA
[8]NASA Ames, Moffett Field, CA, USA

Correspondence to: Susan S. Kulawik (susan.s.kulawik@nasa.gov)

Abstract. We present two new products from near-infrared Greenhouse Gases Observing Satellite (GOSAT) observations: lowermost tropospheric (LMT, from 0 to 2.5 km) and upper tropospheric–stratospheric (U, above 2.5 km) carbon dioxide partial column mixing ratios. We compare these new products to aircraft profiles and remote surface flask measurements and find that the seasonal and year-to-year variations in the new partial column mixing ratios significantly improve upon the Atmospheric CO₂ Observations from Space (ACOS) and GOSAT (ACOS-GOSAT) initial guess and/or a priori, with distinct patterns in the LMT and U seasonal cycles that match validation data. For land monthly averages, we find errors of 1.9, 0.7, and 0.8 ppm for retrieved GOSAT LMT, U, and XCO₂; for ocean monthly averages, we find errors of 0.7, 0.5, and 0.5 ppm for retrieved GOSAT LMT, U, and XCO₂. In the southern hemispheric biomass burning season, the new partial columns show similar patterns to MODIS fire maps and MOPITT multispectral CO for both vertical levels, despite a flat ACOS-GOSAT prior, and a CO–CO₂ emission factor comparable to published values. The difference of LMT and U, useful for evaluation of model transport error, has also been validated with a monthly average error of 0.8 (1.4) ppm for ocean (land). LMT is more locally influenced than U, meaning that local fluxes can now be better separated from CO₂ transported from far away.

1 Introduction

The Greenhouse Gases Observing Satellite (GOSAT) has been measuring global satellite CO₂ columns since 2009, achieving less than 0.3 ppm variability in regional biases and 1.7 ppm single observation error versus the Total Carbon Column Observing Network (TCCON; Kulawik et al., 2016), where the error is estimated as described in Table 3. The sensitivity of near-infrared radiances to CO₂ varies differently by altitude in the strong and weak bands, resulting in the capability of retrieving multiple pieces of vertical information from near-infrared observations, with 3+ degrees of freedom (DOF; i.e., independent pieces of information) for TCCON (Connor et al., 2016; Kuai et al., 2012), 1.6 degrees of freedom for GOSAT (this paper), and 2.0 degrees of freedom for OCO-2 (Kulawik, unpublished result). In this paper we use the intermediate retrieved profile from Atmospheric CO₂ Observations from Space (ACOS) and GOSAT (ACOS-GOSAT), processing to construct, bias correct, and validate two partial column mixing ratios from near-infrared GOSAT
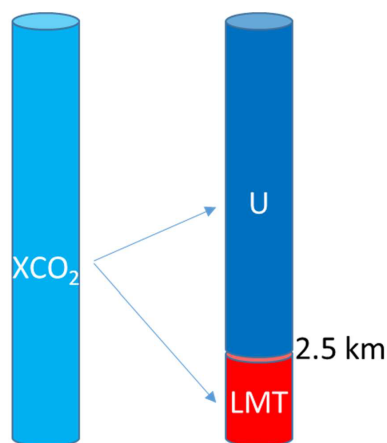
Figure 1. XCO_2 full column measurement (left) and the two partial columns that we introduce (right): the lowermost troposphere (LMT), a partial column from the surface to approximately 2.5 km, and the partial column above 2.5 km (U).

observations (schematically shown in Fig. 1). The partially correlated errors and sensitivity of these two partial column volume mixing ratios (or mole fractions) are characterized so that they can be used for flux estimation and other science analyses.

An important goal of carbon cycle research is to improve top-down estimates of CO_2 fluxes, which assimilate data into models to trace the observed variability in the long-lived tracer backwards to sources and sinks. Historically, such top-down flux estimates have relied on surface observations (e.g., Peters et al., 2007; Chevallier et al., 2010), though it was postulated 15 years ago that satellite-based measurements of column CO_2 could dramatically reduce top-down-based flux uncertainties (Rayner and O'Brien, 2001; O'Brien and Rayner, 2002). Guided by this early work, most GOSAT analyses have focused solely on total column CO_2 (or XCO_2). Separation of XCO_2 into two vertical columns has several advantages over column XCO_2 and surface observations, which should improve our ability to accurately estimate fluxes:

– Flux estimates from column measurements rely on observations up to continental scales away (Liu et al., 2015; Feng et al., 2016), whereas lowermost troposphere (LMT) back trajectories show a more local influence on surface fluxes, making flux estimates more responsive to observations and less susceptible to transport error, a major driver of flux uncertainties (Houweling et al., 2015; Liu et al., 2015, 2011; Chevallier et al., 2014; Prather et al., 2008).

– Stephens et al. (2007) show that vertical gradient in mole fraction determined from two points in the atmospheric column better constrains model transport and partitioning between northern extratropical land fluxes and land fluxes further south since vertical transport is

an uncertainty in flux estimates (Deng et al., 2015; Lauvaux and Davis, 2014; Stephens et al., 2007).

– In the majority of cases, the LMT covers the entire boundary layer, which partially mitigates one source of flask assimilation error, the boundary layer height (Denning et al., 1996; Gurney et al., 2002; Rayner and O'Brien, 2001).

– GOSAT provides observations in many areas that are sparsely covered by surface-based measurements.

In this work, we evaluate the precision and comparability of these new LMT and U partial column products derived from GOSAT, with the goal of providing a higher level of information to the flux inversion estimates than is available from the total column alone. This paper is structured as follows. We introduce the datasets used in Sect. 2 and the theoretical basis in Sect. 3. Section 4 describes methodology, e.g., the coincidence criteria and GOSAT bias correction. Section 4.1 uses back trajectories to estimate the distance to peak sensitivity to surface fluxes for LMT and U. Section 5 shows comparisons to aircraft observations and surface sites, including maps of the two partial column mixing ratios. Section 5.4 shows patterns of the two partial column mixing ratios versus MOPITT multi-spectral CO retrievals, and Sect. 5.5 looks at errors of LMT minus U. Section 6 discusses and summarizes these results.

2   Datasets

There are two datasets used for validation of the new partial column mixing ratios. Measurements of CO_2 vertical profiles from aircraft profiles, which extend from the surface to somewhere between 5 and 13 km, can be used to directly validate what is seen with the two GOSAT partial column mixing ratios. The second dataset that is used is CO_2 measurements from remote surface flask sites, which are used to compare to the lower GOSAT partial column, assuming that CO_2 mixing ratios in the lower 0–2.5 km are well mixed at remote sites. TCCON, which currently measures full columns, is used to diagnose discrepancies between aircraft and GOSAT at the sites where both exist. We additionally show the Southern Hemisphere, which has interesting CO_2 patterns, very little structure in the prior, and no observations used in the bias correction. We show patterns from burning and transport in the Southern Hemisphere from vertically resolved GOSAT, vertically resolved MOPITT CO, and MODIS fire counts. Figure 2 shows aircraft and surface validation locations, along with GOSAT coincidences, with the surface site locations and names shown in Table 1.

2.1   GOSAT

GOSAT takes measurements of reflected sunlight in three near-infrared bands with a circular footprint of approxi-

Table 1. Sites used for validation in this paper.

Type	Site	Site name	Country	Latitude	Longitude	Matches
Aircraft	AOA	Aircraft Observation of Atmospheric trace gases, JMA	Japan	28.8° N	148.4° E	77
Aircraft	BNE	Beaver Crossing, Nebraska	USA	40.8° N	97.2° W	452
Aircraft	CAR	Briggsdale, Colorado	USA	40.4° N	104.3° W	1599
Aircraft	CMA	Cape May, New Jersey	USA	38.8° N	74.3° W	536
Aircraft	DND	Dahlen, North Dakota	USA	47.5° N	99.2° W	415
Aircraft	ESP	Estevan Point, British Columbia	Canada	49.4° N	126.5° W	142
Aircraft	ETL	East Trout Lake, Saskatchewan	Canada	54.4° N	104.9° W	237
Aircraft	HIL	Homer, Illinois	USA	40.1° N	87.9° W	1039
Aircraft	LEF	Park Falls, Wisconsin	USA	45.9° N	90.3° W	717
Aircraft	NHA	Worcester, Massachusetts	USA	42.9° N	70.5° W	430
Aircraft	PFA	Poker Flats, Alaska	USA	65.1° N	147.3° W	107
Aircraft	RTA	Rarotonga	Cook Island	21.3° S	159.8° W	228
Aircraft	SCA	Charleston, South Carolina	USA	32.8° N	79.6° W	764
Aircraft	SGP	Southern Great Plains, Oklahoma	USA	36.6° N	97.5° W	6066
Aircraft	TGC	Sinton, Texas	USA	27.7° N	96.9° W	941
Aircraft	THD	Trinidad Head, California	USA	41.1° N	124.2° W	226
Aircraft	WBI	West Branch, Iowa	USA	41.7° N	91.4° W	602
Surface	MNM	Minamitori Shima	Japan	24.3° N	154.0° E	66 732
Surface	MLO	Mauna Loa, Hawaii	USA	19.5° N	155.6° W	940
Surface	KUM	Cape Kumukahi, Hawaii	USA	19.5° N	154.8° W	876
Surface	GMI	Mariana Islands	Guam	13.4° N	144.6° E	1043
Surface	CHR	Christmas Island	Kiribati	1.7° N	157.2° W	1038
Surface	ASC	Ascension Island	UK	8.0° S	14.4° W	2125
Surface	SMO	Tutuila	American Samoa	14.2° S	170.6° W	4267
Surface	EIC	Easter Island	Chile	27.2° S	109.4° W	432
Surface	SEY	Mahé Island	Seychelles	4.7° S	55.5° E	679
Aircraft	HIPPO 2S	November, 2009; Pacific Ocean		0–39° S	161–178° W	156
Aircraft	HIPPO 2N	November, 2009; Pacific Ocean		6–41° S	151–179° E	277
Aircraft	HIPPO 3S	April, 2010; Pacific Ocean		16° S–14° N	160–170° W	68
Aircraft	HIPPO 3N	April, 2010; Pacific Ocean		16° S–8° N	161–170° W	71
Aircraft	HIPPO 4S	June, 2011; Pacific Ocean		5–15° N	160–164° W	13
Aircraft	HIPPO 4N	July, 2011; Pacific Ocean		4-44° N	134° E–172° W	1054
Aircraft	HIPPO 5S	August, 2011		3° S–15° N	160–166° W	20
Aircraft	HIPPO 5N	September, 2011		18° S–21° N	156–169° W	363
Aircraft	AJAX	California–Nevada	USA	37.3–38.5° N	116–121° W	35

mately 10.5 km diameter at the nadir (Kuze et al., 2016; Yokota et al., 2009; Crisp et al., 2012). The ACOS v3.5 processing of GOSAT XCO$_2$ observations is used from the Lite range of products, with a quality flag of 0 (good), along with the full CO$_2$ profile, full CO$_2$ averaging kernel matrix, and full CO$_2$ error matrices from ancillary GOSAT files. We use both nadir land observations (looking straight down) and ocean glint observations (sunglint tracking mode), but not medium gain over land, as there is not a sufficient number of colocated validation data to validate medium gain observations.

2.2 Aircraft profiles

2.2.1 ESRL aircraft profiles

Aircraft and ocean measurements taken by NOAA's Earth System Research Laboratory (ESRL) are obtained from an observation package product (GLOBALVIEW-CO2, 2013; Sweeney et al., 2015).

2.2.2 Department of Energy (DOE) and Lawrence Berkeley National Laboratory (LBNL) aircraft profiles

Aircraft observations collected over the Southern Great Plains can be obtained from the DOE ARM archive (www.arm.gov, search for CO$_2$ flasks at SGP; see Table 1 for all
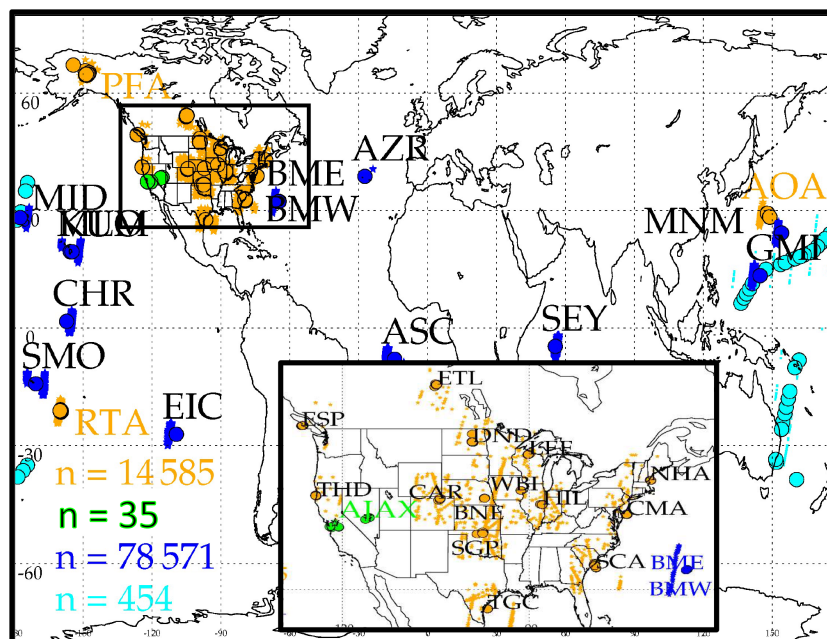
Figure 2. Validation locations. The four sets of validation data shown here are ESRL aircraft profiles (orange), which occur over land (in the US) and ocean (RTA, Rarotonga, and AOA), AJAX aircraft data (green) in the western US, the HIPPO aircraft profiles (light blue), and remote ocean surface sites (dark blue). The matching GOSAT locations are shown as stars and the validation locations are shown as outlined circles. The number of GOSAT observations in each set are shown as the "$n =$" number in the lower left of the plot.

site abbreviations) under ARM–ACME campaigns and are described in Biraud et al. (2013). Flask-based observations are collected twice a week, weather permitting, at an altitude ranging from 0.2 to 5 km.

2.2.3   Aircraft profile extension and errors

Aircraft measurements are extended down to the surface using the lowest measured value, and extended to the tropopause pressure using the aircraft value at the highest altitude. The tropopause pressure is used from the National Centers for Environmental Prediction (NCEP, http://www.esrl.noaa.gov/psd/data/gridded/data.ncep.reanalysis.html). The CarbonTracker model (CT2015, see below) is used to extend the profile through the stratosphere. The aircraft flask measurements themselves have errors, but these are small compared to the other errors in the comparisons (e.g., colocation, extending the aircraft to the top of the atmosphere)

2.3   Remote NOAA/ESRL oceanic surface in situ measurements

Remote surface sites are from the Earth System Research Laboratory Observation Package Data Product surface flask measurements (Conway et al., 1994). The "remote oceanic" locations used in this paper are selected to have at least 97 % ocean along a circle with a 5° radius around the location. The locations are shown in Fig. 2 and Table 1. For each sta-

tion, there can be different options represented by file names (e.g., daytime, nighttime, representative); in this study "representative" files are used, with outliers removed if that option is available. Remote ocean sites have been selected because (a) although the vertical air mass observed by GOSAT LMT will not match the vertical air mass observed by the surface site, the long correlation length scales of remote locations should make the comparisons useful, and (b) these sites are not used in development of the bias correction terms (described in Sect. 3.5 and Appendix A) and so are an independent test of bias correction for observations over ocean.

2.4   HIPPO aircraft profiles

The HIAPER Pole-to-Pole Observations (HIPPO) project samples the atmosphere in a series of profiles from the surface to 9–13 km, from about 80° N to 60° S. The campaigns covered different years as well as different seasons, namely HIPPO 1: January 2009, HIPPO 2: November 2009, HIPPO 3: March–April 2010, HIPPO 4: June–July 2011, and HIPPO 5: August–September 2011. The northbound and southbound legs of HIPPO campaigns were separately analyzed in this paper, e.g., 3S corresponds to the southbound leg, occurring 27 March–7 April 2010, and 3N corresponds to the northbound leg, occurring 7–16 April 2010. Frankenberg et al. (2016) were recently successful in evaluating satellite measurements of column CO_2 over ocean (including GOSAT) using HIPPO. In this paper, we look at comparisons

between GOSAT and HIPPO 2–5 (HIPPO 1 occurs prior to GOSAT launch) using the HIPPO-identified profiles and the CO2_X field, based on 1 s data averaged to 10 s, from two (harmonized) sensors: CO2-QCLS and CO2-OMS. Due to the GOSAT glint coverage span of about 40°, and after applying quality screening, many of the comparisons had fairly limited latitudinal spans, with the GOSAT improvement over the prior found more in improving the bias rather than improving the standard deviation. The combined campaigns span a wide range of GOSAT latitudes.

2.5 AJAX aircraft profiles

The Alpha Jet Atmospheric Experiment (AJAX) project (https://earthscience.arc.nasa.gov/ajax) collects in situ CO_2 vertical profiles from the surface to 8 km in several locations, including Railroad Valley, NV; Merced, CA; and other locations on the west coast. Most of the AJAX Version 4 profiles used in this paper were collected to coincide with GOSAT overpasses. Trace gas instruments and the meteorological measurement sensor are housed in an unpressurized sensor pod that is mounted under the wing. A cavity ring-down spectrometer (Picarro Inc. G2301-m) that has been modified for flight conditions is routinely calibrated to NOAA/ESRL gas standards. Calculated 1σ overall uncertainties are 0.16 ppm for CO_2 (Hamill et al., 2016; Tanaka et al., 2016).

2.6 MOPITT v6 multispectral CO retrieval

In Sect. 5, we utilize satellite-based CO observations from Measurement of Pollution in the Troposphere (MOPITT) to understand the spatial variability in LMT and U that may be attributed to fires. The MOPITT instrument on EOS-Terra is in a sun-synchronous orbit with mean local time overpasses of 10:30 and 22:30. It has global coverage in ~ 3 days with a 22 km $\times$ 22 km horizontal footprint. MOPITT uses gas filter correlation radiometry (GFCR) to measure atmospheric CO at 4.6 μm (thermal infrared) and 2.3 μm (shortwave infrared) and is the only satellite instrument capable of simultaneous multispectral retrievals of CO with enhanced sensitivity to near-surface CO for daytime land observations (Worden et al., 2010). MOPITT CO data have been validated for each retrieval algorithm version using aircraft in situ measurements (Deeter et al., 2014). Here we use only daytime MOPITT V6J (multispectral) data that have been filtered to require cloud free scenes from both MOPITT and MODIS cloud detection. We also use a measure of sensitivity to near-surface CO computed from the trace of the averaging kernel for the lowest 200 hPa of the atmosphere to select scenes that contain relatively more information from the measurement.

2.7 MODIS fire counts

MODIS fire counts (found at https://lance.modaps.eosdis. nasa.gov/cgi-bin/imagery/firemaps.cgi) are used to identify biomass burning locations. Fire maps are created by Jacques Descloitres with a fire detection algorithm developed by Louis Giglio. Blue marble background image created by Reto Stokli (Giglio et al., 2003; Davies et al., 2004).

2.8 CarbonTracker model

CarbonTracker CT2015 (http://carbontracker.noaa.gov; Peters et al., 2007) is used to extend aircraft profiles from the stratosphere to the top of the atmosphere (similarly to in Frankenberg et al., 2016 and Inoue et al., 2013) and to quantify colocation error (similarly to Kulawik et al., 2016).

2.9 TCCON

TCCON observations, version GGG2014 (Wunch et al., 2011a) at Lamont (Wennberg et al., 2014b) and Park Falls (Wennberg et al., 2014a), where both aircraft and TCCON observations have colocated measurements, are used to evaluate XCO_2 calculated from the aircraft observations (extended as described by Sect. 3.7). Although the TCCON observations contain information that allows each measurement to be split into two or three vertical columns, the focus of the TCCON project has been on column observations of CO_2 (and columns of other trace gases). Recent work by Kuai et al. (2012), Dohe et al. (2013), and Connor et al. (2016) has explored vertical profile retrievals from TCCON, but there is not yet an operational product.

2.10 AirCore

While the boundary layer and lower free troposphere are relatively well sampled by a network of in situ and flask measurements over the globe, the upper troposphere and lower stratosphere (UT–LS) is rarely sampled due to the expense and the difficulty involved in making measurements at these altitudes. The recent advent of the AirCore (Karion et al., 2010; Membrive et al., 2016) has enable more frequent profiles that sample as high as 30 km, well into the stratosphere. Profiles in this study were dried with MgClO4 and captured in a long stainless steel tube coated with a thin silicate layer (Silconert 1000) and later (within 3 h of sampling) analyzed for CO_2, CH_4, and CO. Given the 3 h time interval between sampling and analysis of the AirCore and the average rate of molecular diffusion of CO_2, the resolution of the AirCore is better than 1 kPa for the bottom 95 % of the atmospheric column. AirCores were used in Appendix A to estimate the error incurred by extending aircraft CO_2 profiles above 6 km.

3 LMT and U theoretical basis

In Sect. 3.1, equations are presented describing the sensitivity and errors of the new products. In Sect. 3.2, a simulation is shown of what GOSAT is expected to see from space using

the developed equations and aircraft profiles from the Southern Great Plains (SGP) aircraft site.

3.1 Equations describing sensitivity and errors

The ACOS retrievals (O'Dell et al., 2012) utilize an optimal estimation approach with a priori constraints (Rodgers, 2000). It is common practice to represent the state parameter to be retrieved on an altitude grid that is finer than the altitude resolution of the instrument (e.g., Bowman et al., 2006; Deeter et al., 2003; von Clarmann et al., 2003). A major advantage of this approach is that it allows the calculation of diagnostics, such as averaging kernels, which can be used to characterize the sensitivity of the measurement. Constraints (regularization) must be applied in order to stabilize the retrieval (e.g., Rodgers, 2000; Tikhonov, 1963; Twomey, 1963; Steck and von Clarmann, 2001; Kulawik et al., 2006). The constraints may be chosen to constrain absolute values and/or the shape of the retrieved result.

In the ACOS processing, CO_2 is first retrieved as a 20-level profile, where the GOSAT pressure levels are sigma levels, with the fifth level approximately 2.5 km above the surface. The retrieved CO_2 profile averages 1.6 DOF with about 0.8 DOF for levels 16–20 (where level 20 is the surface) and 0.8 DOF for levels 1–15 (where level 1 is at the top of the atmosphere). This intermediate profile has significant altitude-dependent biases and cannot be used scientifically as is, but rather this profile is compacted to a single column quantity, XCO_2, as the final step in the ACOS processing. In this work, we post-process the ACOS-GOSAT intermediate profile to calculate and characterize the partial column mixing ratio represented by levels 16–20, which is named LMT_XCO_2 or LMT for short, and the partial column mixing ratio represented by levels 1–15, which is named U_XCO_2 or U for short. The two partial columns each have about 0.8 DOF, meaning that they will each capture about 80 % of the true variability of their partial column.

The equation for the linear estimate of x, the retrieved CO_2 profile (Connor et al., 2008; Rodgers, 2000), is

$$\hat{x} = x_a + \mathbf{A}_{xx}(x_{\text{true}} - x_a) + \mathbf{A}_{xv}(v_a - v_{\text{true}}) + \mathbf{G}_x \varepsilon, \quad (1)$$

where

- x is the retrieved CO_2 profile, size n_{CO_2} (20 for ACOS-GOSAT);
- x_a is the a priori profile, size n_{CO_2};
- x_{true} is the true value, size n_{CO_2};
- $\mathbf{A}_{xx}$ is the $n_{CO_2} x n_{CO_2}$ CO_2 profile averaging kernel;
- $\mathbf{A}_{xv}(v_a - v_{\text{true}})$ is the cross-state error representing the propagation of error from non-CO_2-retrieved parameters, v (aerosols, albedo, etc.), into retrieved CO_2. This variable is called "u" in Connor et al., 2008;

- v_a is the interferent value (used to generate fit radiances), size n_{interf}. For ACOS-GOSAT n_{interf} is 26 (27) for ocean (land);
- v_{true} is the true interferent value, size n_{interf};
- $\mathbf{A}_{xv}$ is size $n_{CO_2} \times n_{\text{interf}}$;
- $\mathbf{G}_x$ is the gain matrix, size $n_{CO_2} x n_s$, where n_s is the number of spectral points; and
- ε is the spectral error, size n_s.

The pressure weighting function h (size n_{CO_2}) is used to convert the retrieved CO_2 profile to XCO_2 by tracking each level's contribution to the column quantity.

$$h_{XCO_2}^T = [0.026 0.053 0.053 0.053 \cdots 0.053 0.053 0.053 0.026] \quad (2a)$$

The sensitivity to the top or bottom level is half that of other levels as these levels contribute to only one layer, rather than two adjacent layers. The GOSAT levels are chosen such that the pressure weighting is very similar for all layers and all observations. However, the pressure weighting is not identical for all layers and all observations and the values used in our analysis are the actual values in the files, with average values shown here, rounded to two significant digits.

The LMT pressure weighting function is obtained by starting with the pressure weighting function for XCO_2, setting levels 1–15 to zero, then normalizing so that the sum of all entries adds to 1. For the U pressure weighting function, levels 16–20 are set to zero, then the vector is normalized so that the sum is 1. The LMT and U pressure weighting functions are

$$h_{\text{LMT}}^T = [0 0 0 0 \ldots 0 0.22 0.22 0.22 0.22 0.11] \quad (2b)$$
$$h_U^T = [0.035 0.069 0.069 \ldots 0.069 0.069 0 0 0 0]. \quad (2c)$$

To calculate XCO_2, the equation is

$$XCO_2 = h_{XCO_2}^T \cdot \hat{x}. \quad (3)$$

The fraction of total air in each of the partial column averages is

$$f_{XCO_2} = 1 \quad (4a)$$
$$f_{\text{LMT}} = 0.235 \quad (4b)$$
$$f_U = 0.765. \quad (4c)$$

Combining Eqs. (1), (2a), and (3), the XCO_2 estimate is

$$X\hat{C}O_2 = XCO_2 + h_{XCO_2}^T \mathbf{A}_{xx}(x_{\text{true}} - x_a) + h_{XCO_2}^T$$
$$\mathbf{A}_{xv}(v_{\text{true}} - v_a) + h_{XCO_2}^T G_x \varepsilon \quad (5)$$
$$X\hat{C}O_2 = XCO_{2_a} + \mathbf{a}_{xx}(x_{\text{true}} - x_a)$$
$$+ \mathbf{a}_{xv}(v_{\text{true}} - v_a) + \mathbf{g}_x \varepsilon, \quad (6)$$

where a_{xx} is the column averaging kernel, $\mathbf{a}_{xx} = h_{XCO_2}^T \mathbf{A}_{xx}$ (see Appendix A of Connor, 2008).

Similarly, to calculate the linear estimate for the two-vector [LMT, U], Eq. (1) is multiplied by the $2 \times n_{CO_2}$ pressure weighting function, $\boldsymbol{h} = [\boldsymbol{h}_{LMT}, \boldsymbol{h}_U]$:

$$\begin{pmatrix} \hat{LMT} \\ \hat{U} \end{pmatrix} = \begin{pmatrix} LMT \\ \hat{U} \end{pmatrix}_a + \boldsymbol{h}^T \mathbf{A}_{xx} (\boldsymbol{x}_{true} - \boldsymbol{x}_a)$$
$$+ \boldsymbol{h}^T \mathbf{A}_{xv} (\boldsymbol{v}_{true} - \boldsymbol{v}_a) + \boldsymbol{h}^T \mathbf{G}_x \boldsymbol{\varepsilon} \qquad (7a)$$

$$\begin{pmatrix} \hat{LMT} \\ U \end{pmatrix} = \begin{pmatrix} LMT \\ U \end{pmatrix}_a + \mathbf{a}_{xx} (\boldsymbol{x}_{true} - \boldsymbol{x}_a)$$
$$+ \mathbf{a}_{xv} (\boldsymbol{v}_{true} - \boldsymbol{v}_a) + \mathbf{g}_x \boldsymbol{\varepsilon}, \qquad (7b)$$

where now $\boldsymbol{a}_{xx} = [\boldsymbol{h}_{LMT}, \boldsymbol{h}_U]^T A_{xx}$, a $(2 \times n_{CO_2})$ matrix, $a_{xv} = [\boldsymbol{h}_{LMT}, \boldsymbol{h}_U]^T A_{xv}$, a 2 by n_{interf} matrix, and $g_x = [\boldsymbol{h}_{LMT}, \boldsymbol{h}_U]^T G_x$, a $(2 \times n_s)$ matrix.

The last two terms in Eq. (6) represent the cross-state and measurement errors, respectively, and are often jointly called the observation error (Worden et al., 2004). The error in [LMT, U] is estimated by taking the covariance of $\begin{pmatrix} \hat{LMT} \\ \hat{U} \end{pmatrix} - \begin{pmatrix} LMT \\ U \end{pmatrix}_{True}$, a (2×2) matrix. The errors can be calculated either from taking the covariance Eq. (6a) or from Eq. (6b). The covariance of Eq. (6a) has a fairly simple form in terms of the standard definitions of the error covariances for the full profile, S_{interf} and S_{meas}, which are included in the ACOS-GOSAT ancillary products, and $S_{smoothing}$ can be calculated from the standard equation $S_{smoothing} = (\boldsymbol{I} - \boldsymbol{A}) S_a (\boldsymbol{I} - \boldsymbol{A})^T$ (Rodgers, 2000), with $\mathbf{A}$ the $(n_{CO_2} \times n_{CO_2})$ CO_2 profile averaging kernel and S_a the a priori covariance, both included in the ACOS-GOSAT products.

$$\sigma^2_{[LMT,U]} = \boldsymbol{h}^T \mathbf{S}_{smoothing} \boldsymbol{h} + \boldsymbol{h}^T \mathbf{S}_{interfere} \boldsymbol{h} + \boldsymbol{h}^T \mathbf{S}_{meas} \boldsymbol{h} \quad (8a)$$

$$= \begin{pmatrix} \boldsymbol{h}^T_{int} \mathbf{S}_{smooth} \boldsymbol{h}_{int} & \boldsymbol{h}^T_{int} \mathbf{S}_{smooth} \boldsymbol{h}_U \\ \boldsymbol{h}^T_U \mathbf{S}_{smooth} \boldsymbol{h}_{int} & \boldsymbol{h}^T_U \mathbf{S}_{smooth} \boldsymbol{h}_U \end{pmatrix} \quad (8b)$$

$$+ \begin{pmatrix} \boldsymbol{h}^T_{int} \mathbf{S}_{obs} \boldsymbol{h}_{int} & \boldsymbol{h}^T_{int} \mathbf{S}_{obs} \boldsymbol{h}_U \\ \boldsymbol{h}^T_U \mathbf{S}_{obs} \boldsymbol{h}_{int} & \boldsymbol{h}^T_U \mathbf{S}_{obs} \boldsymbol{h}_U \end{pmatrix}$$

$$= \begin{pmatrix} \sigma^2_{LMT} & c \cdot \sigma_{LMT} \sigma_U \\ c \cdot \sigma_{LMT} \sigma_U & \sigma^2_U \end{pmatrix} \quad (8c)$$

Equation (7) estimates the predicted errors for LMT and U, where $\sigma_{[LMT,U]}$ is a (2×2) matrix. The diagonals are the square of the predicted error for each parameter, and the off diagonals also depend on the correlated error, c, between these parameters. Table 2 shows the predicted errors for LMT, U, and the error correlation between LMT and U. The predicted errors in Table 2 are larger than the actual errors, as seen later in Tables 4 and 5; error for averaged observations is estimated in Sect. 4.1.1. The a priori errors, calculated from $\sigma^2 = \boldsymbol{h}^T \mathbf{S}_a \boldsymbol{h}$, are 34 and 9 ppm for LMT and U, respectively, which are much larger than the posterior errors, indicating that these quantities are largely unconstrained by the retrieval's prior assumption.

Through the same process as Eqs. (6)–(7), the XCO_2 error is

$$\sigma_{XCO_2} = \boldsymbol{h}^T_{XCO_2} \mathbf{S}_{smooth} \boldsymbol{h}_{XCO_2} = \boldsymbol{h}^T_{XCO_2} \mathbf{S}_{obs} \boldsymbol{h}_{XCO_2}. \quad (9)$$

Table 2. Predicted errors and degrees of freedom for LMT and U. As seen in Table 3, the predicted errors are much larger than the actual errors.

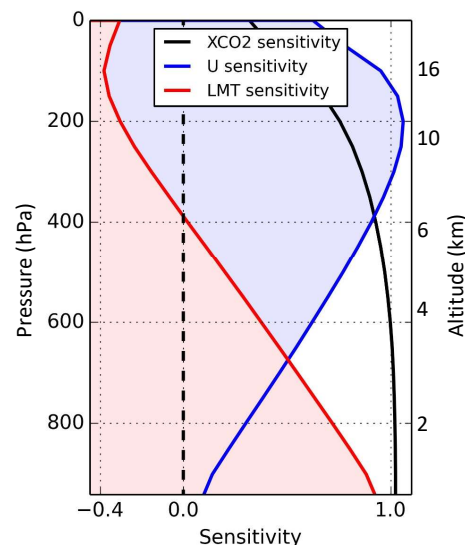|	Land	Ocean
LMT error (ppm)	4.3 ppm	4.4 ppm
U error (ppm)	1.7 ppm	1.7 ppm
U, LMT pred. error correlation	−0.72	−0.78
LMT DOF	0.86	0.86
U DOF	0.84	0.83

Figure 3. Sensitivity of XCO_2 (black), partitioned into the LMT (red) and U (blue) partial columns for an average land averaging kernel. The LMT sensitivity is approximately 1 near the surface and drops off steadily with decreasing pressure.

XCO_2 can also be calculated as a function of LMT and U, and the XCO_2 errors can be calculated as a function of the errors in [LMT, U]. These are shown in Eq. (9).

$$XCO_2 = f_{lmt} LMT_{CO_2} + f_u U_{CO_2} \qquad (10a)$$

$$\sigma_{XCO_2} = \sqrt{\begin{pmatrix} f_{lmt} & f_u \end{pmatrix} \begin{pmatrix} \sigma^2_{lmt} & \sigma_{lmt} \sigma_u \, corr \\ \sigma_{lmt} \sigma_u \, corr & \sigma^2_u \end{pmatrix} \begin{pmatrix} f_{lmt} \\ f_u \end{pmatrix}} \qquad (10b)$$

$$\sigma_{XCO_2} = \sqrt{0.23^2 \sigma^2_{lmt} + \sigma^2_u 0.77^2 + 2 \times 0.77*0.23 \sigma_{lmt} \sigma_u \, corr}, \qquad (10c)$$

where f_{LMT} and f_U are the air masses for the LMT and U partial columns (0.236, 0.764), respectively, σ_{lmt} is the error for LMT, and corr is the error correlation between LMT and U.

The normalized column averaging kernel is used to see the sensitivity of the column to the true state at different levels, with a value of 1 meaning perfect sensitivity and a value of 0 meaning no sensitivity. The normalized column averaging kernel is the column averaging kernel, a, divided by the pressure weighting function for each layer, $\boldsymbol{h}_{XCO_2}$, and mul-

tiplied by the fraction of air in the partial column.

$$a\_norm_{LMT}[i] = (h_{LMT}[i]A_{CO_2}[i, j])/h_{XCO_2}[j] \times f_{LMT} \quad (11a)$$

$$a\_norm_U[i] = (h_U[i]A_{CO_2}[i, j])/h_{XCO_2}[j] \times f_U \quad (11b)$$

Figure 3 shows the normalized column averaging kernels for LMT, U, and XCO_2 for a land scene. The ocean averaging kernel is very similar. Although the LMT partial column mixing ratio sums the five levels within about 2.5 km of the ground, the LMT has some sensitivity to the true state at all 20 levels because the GOSAT radiances are not able to fully resolve between CO_2 within the surface to 2.5 km versus above this. As expected, the sensitivity for LMT plus U is equal to the sensitivity for XCO_2, and the sensitivity for LMT is weighted to the surface, whereas the sensitivity for U is weighted to the top of the atmosphere. The negative averaging kernels for LMT in the stratosphere are partially a consequence of the ACOS prior constraint, which does not allow stratospheric variability. Actual stratospheric variability is transferred to the closest levels that are allowed to vary, and the surface compensates for the radiance error induced by this, resulting in a negative sensitivity of the LMT to the true state in the stratosphere. If the stratospheric truth matches that of the a priori, then there will be no propagation of error into LMT or U. The averaging kernels shown in Fig. 3 are similar to those calculated for TCCON in Fig. 2 of Connor et al. (2016). As seen in Fig. 3, the quantity LMT + U (i.e., XCO_2) has a sensitivity of 1 between the surface and 600 hPa, with sensitivity dropping off slowly with altitude above 600 hPa. The 0.8 DOF for LMT indicates the sensitivity of the retrieved LMT to the true LMT. The missing 0.2 DOF indicates sensitivity to the prior and/or sensitivity to the U part of the true profile. Since the sensitivity of LMT and U together is 1 near the surface, it is mainly sensitivity to the U part of the true profile. Similarly the 0.8 DOF for U indicates some sensitivity to the LMT and some sensitivity to the U prior.

3.2 Seasonal behavior of LMT, U, and XCO_2 estimated using only aircraft measurements and GOSAT sensitivity (no GOSAT observations)

This section answers the following questions:

1. Do U and LMT have unique seasonal signatures?

2. How much of the XCO_2 variability is due to LMT versus U variability?

3. How much does the prior influence the LMT and U retrievals?

This section simulates GOSAT retrievals using the linear estimate given the aircraft in situ profiles at the SGP site (37° N, 95° W), the GOSAT prior, and the GOSAT averaging kernels. This analysis assumes that the CO_2 profile measured by aircraft at SGP (extended by the CarbonTracker
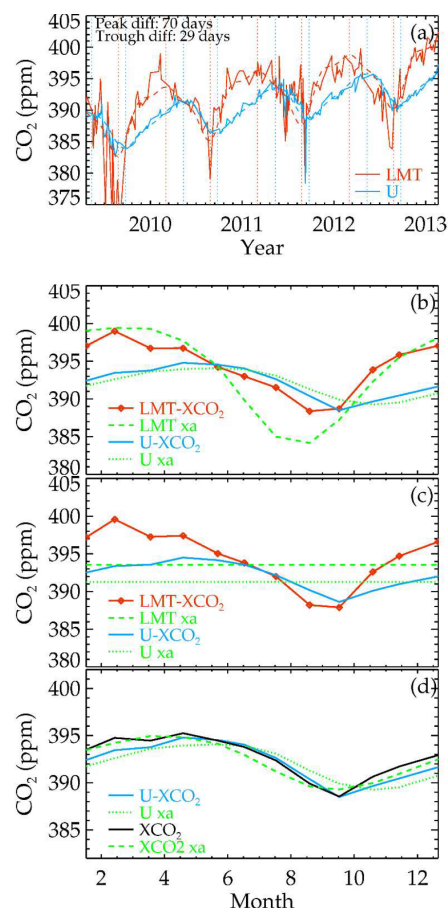

Figure 4. Simulated GOSAT retrievals from SGP aircraft profiles, Eqs. (5)–(6), and the GOSAT averaging kernels. **(a)** Time series of LMT (red) and U (blue) with monthly averages of LMT (red dashed) and U (blue dashed); **(b)** seasonal cycle, averaging in 1-month increments. Green dotted and dashed lines are the initial guess or a priori (xa). **(c)** Same as **(b)** except that the prior is set to a constant, showing that LMT and U results are not strongly influenced by the prior. **(d)** Same as **(b)** but showing U (blue) and XCO_2 (black).

model above 5.5 km) is the true CO_2 profile, which is then plugged into Eqs. (5) and (6) to calculate the LMT and U that GOSAT would see at the SGP site, using the GOSAT averaging kernels and priors. The measurement error and interference terms are assumed to be zero for this analysis.

Using this analysis, the importance of the prior is assessed by using either a prior that is constant in location and time (with only a 2 ppm yr^{-1} secular increase) or the GOSAT prior, in Eqs. (5) and (6). We assess how much LMT and U contribute to the variations seen in XCO_2 using the variability of the LMT and U partial columns combined with the weighting each has in the full column. The seasonal cycles of each partial column mixing ratio are studied by adjusting all aircraft measurements at SGP (2009 to 2014) to a common year (2012) by applying a 2 ppm yr^{-1} secular trend and

Table 3. Definition of comparison terms.

Colocation bias: the mean difference of CarbonTracker matched to the satellite minus CarbonTracker matched to the aircraft. A persistent colocation bias indicates sampling differences. For example, a seasonal colocation error was found to result from time-of-day difference between validation data collection time and the GOSAT overpass (see Fig. 11). For ocean flasks, where the validation data are only at the surface, vertical colocation bias of 0.3 ppm results from sampling difference between the model sampled with the LMT averaging kernel and the model at the surface (see Table 4).
Colocation error, $\varepsilon_{\text{coloc}}$: the standard deviation of CarbonTracker matched to the satellite minus CarbonTracker matched to the aircraft or surface flask. This represents error introduced by the satellite not observing at the exact time and location of the validation data. The surface flasks have an additional term, the standard deviation of CarbonTracker sampled with the LMT averaging kernel and CarbonTracker sampled at the surface.
Correlated error: correlated error is the component of the standard deviation that does not reduce when additional GOSAT observations are averaged. Think of this quantity as a regional, daily (or a bit longer) bias. See Eq. (11).
Random error: random error is the component of the standard deviation that reduces when more GOSAT observations are averaged. See Eq. (11).
GOSAT bias: the mean of GOSAT minus the validation data. The bias is calculated by latitude, season, and time. Different biases at different locations can cause phantom fluxes.
GOSAT error: the standard deviation of GOSAT minus the validation data.
Predicted error: the error predicted by the GOSAT optimal estimation retrieval system.
Prior bias: the mean of the GOSAT prior minus the validation data.
True mean: the mean of all validation data at that site. For stations, the mean is averaged over time, and for each HIPPO campaign, it is averaged over latitude and longitude.
True variability: the standard deviation of the validation data for each station or campaign. The true variability is higher over land than ocean, or for the LMT versus U. Observations with larger error will be more useful at locations where there is higher true variability.
$(n = 1)$, $(n = 15)$: this specifies how many GOSAT observations are averaged prior to the calculation of bias or error. All GOSAT observations that are averaged match the same validation data point. The size of n matters for errors, with larger averaged numbers resulting in smaller errors (but not reducing as fast as the square root of n).

binning all observations by month. This method was used rather than fitting the aircraft observations using the NOAA fitting routine (CCGCRV; described in Thoning et al., 1989) to estimate the seasonal cycle shape because we found that the aircraft observations (matched to GOSAT and within the GOSAT record) are not sufficiently smooth to result in a consistent fit. Figure 4 shows the estimates of LMT, U, and XCO$_2$ using SGP aircraft profiles calculated as described above. There is significant variability in the individual aircraft measurements, seen in panel (a), but this is smoothed out on monthly timescales, seen in the remaining panels. The dashed lines in panel (a) represent fits using the NOAA fitting software CCGCRV. Single U partial column mixing ratios are rarely more than 1 ppm different from the fit, whereas single LMT mixing ratios can be up to 5 ppm different (e.g., see summer, 2009; January, 2010; summer, 2011).

Figure 4b and c show the difference between the simulated retrievals with the GOSAT a priori (b) versus a flat a priori (c) for the seasonal cycle. The patterns are very similar, indicating that the signal is primarily coming from the data rather than the prior, with standard deviations of 0.8 ppm for LMT and 0.3 ppm for U (these changes are fully characterized when applying the GOSAT prior to the aircraft true profile with the specified a priori vector).

Figure 4d shows U versus XCO$_2$. At first glance U and XCO$_2$ look very similar, but by comparing panels (d) and (b), the XCO$_2$ deviations move towards LMT relative to the prior. The seasonal variabilities of XCO$_2$, LMT, and U (maximum minus minimum) are 3.3, 4.8, and 3.3 ppm, respectively. Note that the seasonal variations in LMT and U have a 0.56 correlation, suggesting some independence between these two variables. A straightforward calculation of variation times air fraction (Eq. 4) shows that the fraction of variation of XCO$_2$ resulting from variations in LMT is approximately 30 %, and the fraction of the variation in XCO$_2$ coming from U variation is roughly 70 %. It is expected that U has the much larger impact on XCO$_2$ due to the fact that the full column is 77 % LMT. A similar calculation at Park

Table 4. Biases versus validation data. See Table 3 for terminology used in this table. Note that all data are averaged by location or campaign. The ± represents the variability of the bias by location or campaign, a key metric in the data quality.

	Type	Ocean surface (ppm)	HIPPO ocean (ppm)	ESRL ocean (ppm)	ESRL land (ppm)	AJAX land (ppm)
Colocation bias	LMT	-0.3 ± 0.3 -0.3 ± 0.8	-0.3 ± 0.2	-0.3 ± 0.4	-0.6 ± 0.7	-0.6
	U		0.1 ± 0.1	-0.1 ± 0.1	0.0 ± 0.2	0.0
	$X\mathrm{CO_2}$		0.0 ± 0.1	-0.1 ± 0.1	-0.1 ± 0.3	-0.1
True mean	LMT	391.3 ± 1.6	392.2 ± 1.6	391.7 ± 1.1	392.2 ± 3.1	393.6
	U		391.1 ± 1.2	391.3 ± 1.6	391.2 ± 0.6	392.2
	$X\mathrm{CO_2}$		391.4 ± 1.3	391.4 ± 1.5	391.5 ± 1.1	392.4
Prior bias	LMT	-0.8 ± 1.5	0.1 ± 2.4	-1.5 ± 4.5	-0.4 ± 1.2	-1.4
	U		1.2 ± 0.1	-1.2 ± 1.6	0.6 ± 0.6	0.4
	$X\mathrm{CO_2}$		0.9 ± 1.4	0.4 ± 2.3	-0.2 ± 0.6	-0.1
GOSAT bias	LMT	1.1 ± 1.1	0.1 ± 0.3	0.3 ± 0.7	-0.2 ± 1.0	0.4
	U		0.1 ± 0.3	0.7 ± 0.1	0.3 ± 0.9	1.0
	$X\mathrm{CO_2}$		0.1 ± 0.2	0.6 ± 0.4	0.1 ± 0.9	0.7

Table 5. Standard deviations versus validation data. See Table 3 for definitions of terms. The colocation errors have been subtracted out from the GOSAT errors.

	Type	Ocean surface (ppm)	HIPPO ocean (ppm)	ESRL ocean (ppm)	ESRL land (ppm)	AJAX land (ppm)
Colocation error	LMT	0.5 ± 0.2 0.9 ± 0.4	0.3 ± 0.1	0.3 ± 0.1	2.1 ± 0.7	1.1
	U		0.1 ± 0.1	0.2 ± 0.0	0.5 ± 0.3	0.1
	$X\mathrm{CO_2}$		0.1 ± 0.2	0.2 ± 0.1	0.8 ± 0.3	0.2
Predicted error ($n = 1$)	LMT	4.3 ± 0.2	4.3 ± 0.3	4.3 ± 0.1	4.6 ± 0.3	4.1
	U		1.7 ± 0.1	1.7 ± 0.0	1.8 ± 0.0	1.7
	$X\mathrm{CO_2}$		0.6 ± 0.1	0.7 ± 0.1	0.9 ± 0.1	0.8
GOSAT error ($n = 1$)	LMT	1.7 ± 0.4	1.7 ± 0.3	1.5 ± 0.1	3.4 ± 0.7	2.9
	U		0.8 ± 0.1	0.8 ± 0.0	1.3 ± 0.3	1.1
	$X\mathrm{CO_2}$		0.9 ± 0.1	0.8 ± 0.1	1.7 ± 0.4	0.9
True variability	LMT	1.3 ± 0.8	0.6 ± 0.2	0.9 ± 0.6	5.5 ± 2.0	2.8
	U		0.4 ± 0.3	0.8 ± 0.8	2.0 ± 0.2	2.0
	$X\mathrm{CO_2}$		0.3 ± 0.3	0.8 ± 0.8	2.5 ± 0.6	2.4
Prior error ($n = 15$)	LMT	2.2 ± 0.9	0.5 ± 0.3	0.7 ± 0.2	2.1 ± 1.0	–
	U		0.3 ± 0.1	0.5 ± 0.0	0.9 ± 0.2	–
	$X\mathrm{CO_2}$		0.3 ± 0.1	0.5 ± 0.1	1.1 ± 0.6	–
GOSAT error ($n = 15$)	LMT	0.4 ± 0.3	0.5 ± 0.1	0.4 ± 0.1	1.9 ± 1.1	–
	U		0.4 ± 0.1	0.6 ± 0.1	0.7 ± 0.4	–
	$X\mathrm{CO_2}$		0.3 ± 0.1	0.4 ± 0.1	0.8 ± 0.5	–

Falls, where the LMT seasonal cycle is 20 ppm and the U seasonal cycle is 5 ppm, finds that 45 % of the seasonal variability in $X\mathrm{CO_2}$ results from U and 55 % from LMT at Park Falls (46° N). Here, the high variability in LMT will have a much larger impact on $X\mathrm{CO_2}$ despite the fact that it represents a smaller part of the column.

Figure 4 indicates that LMT and U do have unique seasonal cycles, which result from the data rather than the prior. The LMT partial column, which contributes to 30 % of the variations observed in $X\mathrm{CO_2}$, has a much larger seasonal variability than the U partial column or the $X\mathrm{CO_2}$ column, and it has earlier seasonal cycle maximums and minimums.

4 Methods

We test the sensitivity of the new products to surface fluxes using back-trajectory footprints in Sect. 4.1. Section 4.2 discusses how GOSAT is compared to aircraft. Section 4.3–4.5 describe the bias correction, how the aircraft data are extended to the full atmosphere, and the coincidence criteria.

4.1 Sensitivity of the LMT and U partial column mixing ratios to surface fluxes

To compare LMT and U sensitivity to surface fluxes, we look at 10-day back-trajectory footprints created using the Weather Research and Forecasting (WRF) model combined with the Stochastic Time-Inverted Lagrangian Transport (STILT) model (WRF-STILT; Nehrkorn et al., 2010). The "footprint" for an observation is a map of the surface locations to which an observation is sensitive. Footprints are created for each of the 20 GOSAT levels and are then convolved with the LMT and U averaging kernels. The averaging kernel estimates the sensitivity of the GOSAT measurement of each quantity to the true state at each level. Footprint maps are created that show the sensitivity of each type of GOSAT observation to sources and sinks. This was done for 10 GOSAT observations in the Amazon. The average distance for the nearest 10 % of footprints is 260 km for LMT and 790 km for U. It is likely that there is also a very long tail in the U sensitivity, based on the work of Liu et al. (2015) and Feng et al. (2016).

4.2 Comparisons to aircraft

The correct way to validate GOSAT estimates of [LMT, U] is to compare the GOSAT observations to an estimate of what GOSAT should observe, given its sensitivity, when the true atmospheric state is set to the aircraft CO_2 profile using Eq. (6). The agreement should be within the GOSAT observation error as the smoothing term's effects on the comparison are removed by the application of the GOSAT averaging kernel to the validation data. The aircraft measurements are assumed to be unbiased and have a small measurement error compared to the errors in the GOSAT profiles.

4.3 GOSAT bias correction

The GOSAT standard XCO_2 product has regional biases and errors, which can be partially corrected using jointly retrieved parameters, pre-filters, or radiance properties (e.g., the ratio of the signal in the strong vs. weak band, retrieved albedo slopes or values, retrieved aerosol slopes or values) and through post-processing screening, e.g., removing fits where the difference in the retrieved versus prior surface pressure is greater than 4 hPa. We apply the same techniques to the LMT partial column mixing ratio in Appendix A, which is briefly described here. After LMT is corrected, the corrected U partial column mixing ratio is set using Eq. (9a)

so that XCO_2 is consistent with LMT and U. The purpose of setting U this way is that (a) there is a lack of validation data for the U partial column; thus, bias correction would be a lot less certain, and (b) it is useful to have the new products be consistent with current operational column results.

To correct the LMT partial column mixing ratio, a set of pairs of true and retrieved values is compiled using validation data. GOSAT minus true is plotted versus various GOSAT parameters described in Appendix A, and if a slope is found for the GOSAT error versus any parameter, then a correction is applied for that parameter. The robustness of the correction is tested by verifying the correction on data withheld from the fit, as described in Appendix A. Following the initial bias correction, GOSAT LMT is compared for closely occurring ocean and land pairs; a constant bias term is added to the land bias correction so that land and ocean, on average, are consistent.

4.4 Coincidence criteria

"Geometric criteria", defined as ±3° latitude, ±5° longitude ±1 week time, are used to select coincident GOSAT observations for particular sites. For GOSAT criteria, 5° latitude–longitude, 1 h has previously been used (Kulawik et al., 2016); however, this did not yield enough matches for aircraft profiles. With the criteria above, the total matches range from 64 (at Poker Flats, station ID PFA) to 4800 (at the Southern Great Plains, station ID SGP), with median 430, which is approximately 9 months, assuming all months are equally well sampled throughout the time series. A tight spatial criteria was selected to best capture the seasonal cycle at a given location, especially for land where spatial variability is large. Because aircraft and surface observations are more infrequent than TCCON, an extended temporal window was used for the comparisons to obtain sufficient comparison data. Other methods that were tried were dynamic coincidence criteria (Wunch et al., 2011b), which consider a larger area (±10° latitude, ±30° longitude) but also match atmospheric temperature, and a variant of Basu criteria (Guerlet et al., 2013), which used dynamic coincidences, which had model–model differences less than 0.5 ppm. All three criteria gave similar results overall, with different criteria performing better at different stations, but there was no clear overall best criteria. For HIPPO data, which mainly test latitude gradients over ocean, the dynamic coincidence approach was used following Frankenberg et al. (2016). Different variations on the dynamic coincidence criteria were tested, e.g., using temperature comparisons at the surface, averaging from the surface to 2.5 km, or weighting temperature differences by the pressure weighting function. The different temperature criteria yielded similar results overall, other than using temperature differences at the surface, which did not work as well as the other levels. We therefore used the standard dynamic criteria from Wunch et al. (2011b).
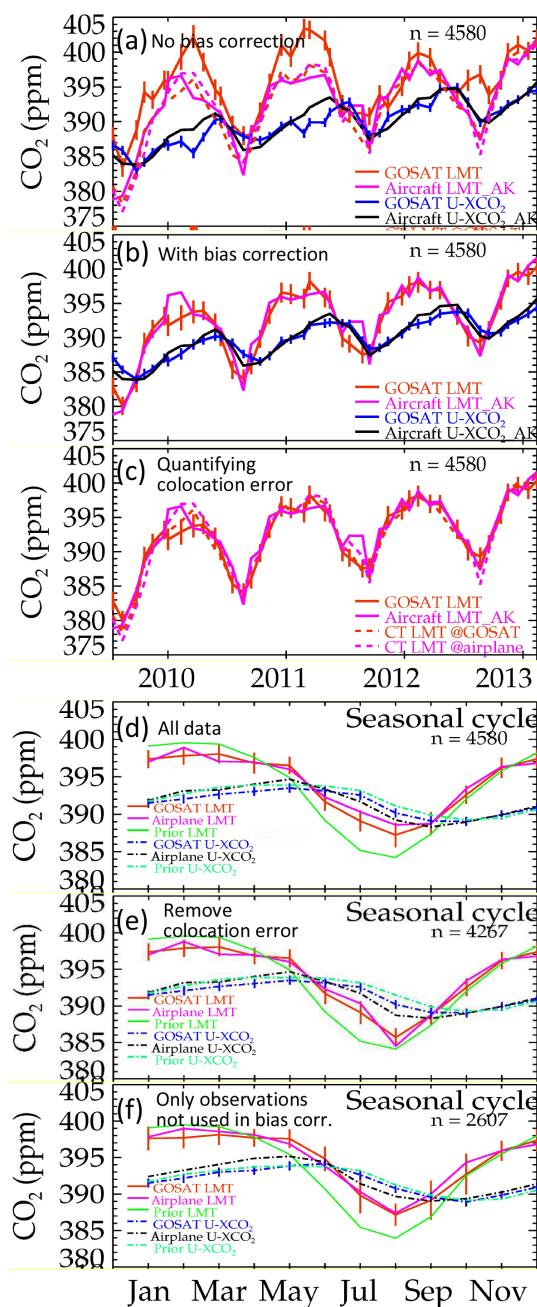
Figure 5. GOSAT versus aircraft data at the SGP site ($37°$ N, $95°$ W). **(a, b, c)** Aircraft LMT (pink) and U (blue) versus GOSAT LMT (red) and U (black) for monthly averages of GOSAT and airplane matches. **(a)** Using no bias correction, **(b)** using bias correction factors derived in Appendix A. **(c)** Also showing CarbonTracker matched to GOSAT (red dotted) and CarbonTracker matched to aircraft (pink dotted) for LMT. **(d)** Seasonal cycle of GOSAT and airplane, same colors as top panels, and adding the priors in green. **(e)** Seasonal cycle, but removing months where the CarbonTracker differences seen in **(b)** are larger than 2.5 ppm. **(f)** Same as **(e)** but with observations used in the bias correction removed from the comparison.

4.5 Extension of the aircraft profile

The aircraft measurements go from the surface to between 5.5–8 km for most ESRL land and 9–13 km for HIPPO observations. As GOSAT LMT, U, and XCO_2 have sensitivity above 5.5 km and even above 13 km, as seen in the averaging kernel shown in Fig. 3, the aircraft profile needs to be extended from the top measurement to the top of the atmosphere. Four different methods of extension were tested: extending with the GOSAT prior, extending the top aircraft measurement through the tropopause pressure and extending with the GOSAT prior above this, extending with the CT2015 model, and extending the top aircraft measurement through the tropopause pressure and extending with the CT2015 model above this. The different extensions mainly had an effect on the overall LMT, U, and XCO_2 biases rather than the standard deviation, with a spread of 0.4 ppm, as seen in Table A4. The extension that was used in the rest of the paper is extending the top aircraft measurement through the tropopause pressure and extending with the CT2015 model above this. There was no clear winner on the profile extension, and this choice was just a preference.

5 GOSAT results

Figure 5 shows GOSAT comparisons for LMT and U versus the aircraft measurements at the SGP site at $37°$ N, $95°$ W, which can be compared to the simulated results shown in Fig. 4. The GOSAT LMT and U products show the same seasonal patterns as seen in the aircraft data. Figure 5a shows results without bias correction (though we do apply a constant 12 ppm correction to LMT). The GOSAT results show a similar seasonal cycle to the aircraft but with large and temporally correlated errors. Figure 5b shows the results with the bias correction as described in Appendix A. Figure 5c shows CarbonTracker matched to GOSAT (CT@GOSAT) and CarbonTracker matched to the aircraft measurements (CT@aircraft). The difference of CT@GOSAT and CT@aircraft estimates the colocation error. Large differences are seen between CT@GOSAT and CT@aircraft in early 2010; summer, 2010; and summer, 2011. In Fig. 5d, the seasonal cycle is shown by transforming all data to lie within 2012 using $2\,\mathrm{ppm\,yr^{-1}}$ adjustment to CO_2. There are systematic differences seen in the drawdown, which is underestimated by GOSAT. However, when months that have differences of (CT@GOSAT-CT@aircraft) more than 2.5 ppm are removed (removing June, 2009; October, 2009; May, 2010; July, 2010; and August, 2010), Fig. 5e shows agreement within the GOSAT predicted errors between GOSAT and aircraft. Figure 5f is the same as Fig. 5e but removes all observations that were used to develop the bias correction. There is no significant difference between Fig. 5f and e. The authors have some concerns about applying the bias correction to parts of the world where there are

not validation data, e.g., the land bias correction was primarily used over the US. Similarly, the HIPPO observations used for ocean bias correction are in the Pacific Ocean; thus, the ocean bias correction in the Atlantic Ocean is less certain.

GOSAT U improves over the a priori for actual observations (Fig. 5d–f) and in simulated (Fig. 4b) results. This is shown by the black (aircraft) vs. blue (GOSAT) in Fig. 5c, where there is better agreement in July–November than prior (green) vs. black (aircraft). The bias seen in the U partial column mixing ratio versus the aircraft U estimate is also found in XCO_2 versus the aircraft.

5.1 Summary of comparisons to all validation data

GOSAT LMT, U, and XCO_2 are compared to aircraft profiles, where the aircraft profile has the GOSAT averaging kernel applied so that the sensitivity is considered. The comparison locations are shown in Fig. 2. More detailed comparisons, showing results for each location and/or campaign, are shown in Appendix B. Definitions of the quantities calculated and compared are shown in Table 3.

Table 4 shows the biases with respect to aircraft data and Table 5 shows the standard deviation with respect to aircraft for single and averaged observations. The bias or standard deviation is calculated for every site (or campaign). The mean represents the average of all site means, and the ± represents the standard deviation for the means averaged by site (or campaign). The variability of the bias by location or time is a key metric in the data quality. Biases that vary by season or location cannot be corrected for and will be particularly detrimental to the use of satellite data for inverse flux estimates as the assimilation will attribute these biases to spurious fluxes.

The colocation error is estimated by comparing CarbonTracker to itself at the satellite location and time and CarbonTracker at the aircraft location and time. For the ocean surface sites, a vertical colocation error is estimated by comparing CarbonTracker with the LMT averaging kernel to CarbonTracker at the surface. In Tables 4–6, the top entry in the ocean surface colocation error is from discrepancies in horizontal location and time. The bottom entry is the colocation error for sampling CarbonTracker for the LMT quantity versus CarbonTracker at the surface.

5.1.1 Bias

In Table 3, the colocation bias is largest for aircraft land, with an overall bias of −0.6 ppm and bias variability of 0.7 ppm. This gives an approximate best case of what could be achieved by GOSAT–aircraft comparisons. An investigation of the −2 ppm colocation bias in the LMT partial column mixing ratio at CAR in July (during the drawdown) finds that the GOSAT observations are always taken 3–4 h later than the aircraft. The CarbonTracker model estimates the effect of +3 h as resulting in a −2 ppm change in the LMT par-

tial column mixing ratio. The colocation bias reflects spatial, diurnal, and seasonal colocation errors. Taking out the five sites that have colocation biases > 0.5 ppm (see Appendix B, Table B1: WBI, BNE, CAR, HIL, and CMA) reduces the colocation bias to −0.2 ± 0.3 ppm.

In Table 4, the true mean by site or campaign is the mean true value averaged by location (or campaign). The ± represents the standard deviation of the mean true value by location (or campaign). The GOSAT retrieval must improve on the ± at the very least to provide information on the atmospheric state. The GOSAT prior bias improves over the true variability on land but not for ocean cases for LMT. For U, the a priori minus true variability is the same size as the true variability. The GOSAT bias improves over the prior in all entries of the absolute bias, except for XCO_2 for ESRL ocean and U and XCO_2 for AJAX. Issues with both U and XCO_2 suggest a possible issue with the profile extension above the aircraft. Improvement over the prior for GOSAT ± bias occurs in all comparisons. Note that for ESRL land, if the five stations with a large colocation error are taken out, the LMT bias variability decreases from 1.0 to 0.7 ppm.

The location-dependent bias is important because this bias variability cannot be easily corrected and will be attributed to phantom fluxes. The LMT location-dependent bias is no worse than the XCO_2 location-dependent bias, whereas the LMT signals are much more variable than XCO_2. The bias variability for XCO_2 and U are possibly too high due to uncertainty of the aircraft profile extension because the bias variability is much larger than the 0.3 ppm seen in Kulawik et al. (2016) versus TCCON. Taking out sites with large colocation bias for XCO_2 does not improve the GOSAT XCO_2 bias variability. Taking out the top four GOSAT XCO_2 bias outliers results in a GOSAT XCO_2 bias variability of 0.5 ppm for the remaining sites; however, these four sites are not the same sites where LMT has bias issues, nor are these sites where CarbonTracker shows a large colocation bias.

5.1.2 Standard deviation

Table 5 calculates errors versus aircraft data. The colocation error gives an upper bound on how well we could expect GOSAT to compare to the observations. The colocation error is subtracted, in quadrature, from the GOSAT error to estimate the GOSAT errors in the absence of a colocation error.

To reduce the colocation error, a very tight coincidence criteria of 2° and 1 h was applied, yielding 146 matches, of which 89 are at SGP and 39 at HIL. Results for these tight coincidences are compared to the looser coincidence criteria results for these sites. For the tighter coincidences, the LMT colocation error is 0.3 and 0.7 ppm at SGP and HIL, respectively, and the GOSAT LMT ($n = 1$) error is 2.6 and 2.5 ppm. This is compared to the looser coincidence results, where LMT colocation error is 1.8 and 2.2 ppm and GOSAT LMT error is 3.9 and 3.8 ppm. This analysis suggests that the colocation error based on CarbonTracker may be underestimated.

Table 6. Estimated colocation, correlated, and random errors using Eq. (12). The colocation errors are taken from Table 4.

	Type	Ocean surface (ppm)	HIPPO ocean (ppm)	ESRL ocean (ppm)	ESRL land (ppm)
Colocation error	LMT	1.0 ± 0.4	0.3 ± 0.1	0.3 ± 0.1	2.1 ± 0.7
	U		0.1 ± 0.1	0.2 ± 0.0	0.5 ± 0.3
	$X\mathrm{CO_2}$		0.1 ± 0.1	0.1 ± 0.1	0.8 ± 0.3
Correlated error (a_o)	LMT	0.4 ± 0.3	0.3 ± 0.2	0.3 ± 0.2	1.7 ± 1.3
	U		0.3 ± 0.2	0.5 ± 0.1	0.6 ± 0.4
	$X\mathrm{CO_2}$		0.2 ± 0.2	0.4 ± 0.1	1.1 ± 0.6
Random error (b)	LMT	1.6 ± 0.4	1.6 ± 0.3	1.4 ± 0.2	3.0 ± 0.6
	U		0.8 ± 0.1	0.6 ± 0.1	1.2 ± 0.1
	$X\mathrm{CO_2}$		0.9 ± 0.1	0.4 ± 0.1	0.8 ± 0.3

The GOSAT LMT ($n = 1$) error in Table 5 for ESRL land (which has colocation error subtracted) is 3.4 ppm, whereas the error when the tighter coincidence criteria are applied is actually much less, 2.6 ppm. For U, the GOSAT ($n = 1$) error is 1.0 and 1.4, whereas it is 1.3 and 1.2 for the looser criteria. Thus, tight versus loose coincidence criteria did not matter a lot for U comparisons.

The next row of Table 5 is the predicted error, given by Eqs. (7) and (9), which is on the order of 4.5 ppm for LMT, 1.7 ppm for U, and 0.7 ppm for $X\mathrm{CO_2}$. The actual standard deviation of GOSAT versus aircraft, however, is about half that for LMT and U and double the predicted error for $X\mathrm{CO_2}$. This is discussed in Sect. 5.1.5.

The true variability in Table 5 shows how much the different partial column mixing ratios vary by month. The variability of LMT over land is 5.4 ppm, about double that of U or $X\mathrm{CO_2}$, and the variability of LMT at remote ocean sites is 1.1 ppm, about 50 % larger than U or $X\mathrm{CO_2}$ variability.

The prior standard deviation ($n = 15$) and GOSAT standard deviation ($n = 15$) look at the error of averaged GOSAT values, which is important for understanding bias that will result from assimilating these data for flux estimates. Kulawik et al. (2016) showed that the GOSAT error does not drop off as the inverse square root of the number of observations, like it would if the error were fully random. The error for 15 observation averages is about 0.4 times that of one observation for land, with a similar factor for $X\mathrm{CO_2}$, LMT, and U, and it is about 0.5 times that of one observation for ocean, similarly for all quantities. Note that the colocation error has been subtracted out (in quadrature) for both the a priori and GOSAT errors.

The standard deviations for LMT, U, and $X\mathrm{CO_2}$ show improvement over the prior for land cases but improve only marginally or do not improve over ocean. The location-dependent bias, however, does show improvement for LMT and U in Table 4. For surface ocean sites, which are only compared to LMT, the improvement over the prior is much

better, mainly because the prior is not very good at these sites.

5.1.3 Errors separated into colocation, random, and correlated error

The errors between aircraft and GOSAT observations can be parametrized by the number of GOSAT observations that are averaged. Kulawik et al. (2016) found that the form in Eq. (11) matched well to the observed errors.

$$\text{error} = \sqrt{a^2 + b^2/n} \tag{12}$$

$$\text{error} = \sqrt{\varepsilon_{\mathrm{coloc}}^2 + a_o^2 + b^2/n}, \tag{13}$$

where n is the number of GOSAT observations that are averaged (all of the averaged observations match a single aircraft measurement), a is error that does not reduce with averaging, and b is the random error. a is further split into colocation error, $\varepsilon_{\mathrm{coloc}}$, plus a_o, the correlated error in Eq. (12). Correlated error means that no matter how many observations are taken, this error does not reduce, which can be due to interferents or spectroscopy in combination with attributes specific to different locations and times.

The colocation error is the error resulting from imperfect matching of the aircraft and satellite observations and is approximated by the standard deviation of the CarbonTracker model at the validation location and time and the model at the satellite observation location and time; it is tabulated in Table 6. This term, as seen in Table 6, is comparable to or even larger than a for LMT land cases. Some colocation schemes (e.g., as implemented by S. Basu described in Guerlet et al., 2013) use the model–model differences to select the best satellite observations to match validation data. Equation (11) is used to determine a and b, and then a_o is calculated from a and $\varepsilon_{\mathrm{coloc}}$.

The colocation error is subtracted from the correlated error to try to remove the effect of colocation on the error estimate. This is a statistical subtraction as no value was found

in subtracting the colocation error for individual comparisons (perhaps because the model is not accurate enough to capture the colocation differences case by case). The three quantities from Eq. (12) are shown in Table 6. For LMT the colocation error is about the same size as the correlated error for ocean, and the colocation error is larger than correlated error for land. For U and $X\mathrm{CO_2}$, the correlated errors are larger than the colocation error for ocean and are comparable for land.

5.1.4 Comparison of $X\mathrm{CO_2}$ results to previous results

We compare GOSAT $X\mathrm{CO_2}$ comparisons to the previous validations using TCCON (Wunch et al., 2011b; Kulawik et al., 2016) and HIPPO observations (Frankenberg et al., 2016). The GOSAT comparisons to HIPPO in Frankenberg et al. (2016) were for at least six averages and did not subtract colocation error (which is only 0.1 ppm over ocean). Using Eq. (12) and Table 6, we find that the $X\mathrm{CO_2}$ error for $n = 6$ is 0.43 ppm, in agreement with 0.45 from Frankenberg et al. (2016). Without colocation error, the $X\mathrm{CO_2}$ from $n = 6$ is 0.42 ppm. For ESRL land, several quantities in Tables 4–6 can be directly compared to previous GOSAT–TCCON validation: the colocation error (0.8 ppm) is larger than colocation for geometric coincidence (0.4 ppm) but smaller than for dynamic coincidence (0.9 ppm) from Kulawik et al. (2016). This makes sense as Kulawik et al. (2016) had a 1 h coincidence with TCCON, whereas 7 days is used in this paper (because aircraft measurements are sparser in time than TCCON observations). a_o and b values of 0.7 ± 0.5 and 1.6 ± 0.2 ppm in this work are consistent with 0.8 ± 0.2 and 1.6 ± 0.1 ppm, for a (corrected) and b, respectively, from Table 2 of Kulawik et al. (2016). Additionally, the predicted error of 0.9 ± 0.1, which is a factor of 1.9 less than the actual error of 1.7 ± 0.4, are identical to the values and relative sizes of predicted versus actual error in Kulawik et al. (2016) at the end of Sect. 3.1.

As discussed in Sect. 5.1.1, the location-dependent bias found in Kulawik et al. (2016) versus TCCON sites for $X\mathrm{CO_2}$ was 0.3 (after removing outlying stations north of 60° N and locally influenced stations). In this paper, we find the bias variability for $X\mathrm{CO_2}$ to be 0.9 ppm over land and 0.3 ppm over ocean (see Table 4). One reason for the discrepancy could be from the extension of the profile above the aircraft measurement (about 5–6 km). As seen in Appendix A, different methods for profile extension cause changes on the order of 0.4 ppm. Another possible cause for the discrepancy is that GOSAT has been extensively tested against TCCON and issues that show up at TCCON locations have been previously addressed. This was tested by fitting bias correction factor for U specifically, rather than calculating bias-correction factors for LMT and subtracting the LMT partial column from GOSAT $X\mathrm{CO_2}$ to estimate U. The bias variability for U did not improve when bias correction factors were calculated directly for U. We also compare GOSAT

$X\mathrm{CO_2}$ aircraft comparisons and GOSAT $X\mathrm{CO_2}$ comparisons to TCCON at the two sites where both validation data are colocated: Park Falls, Wisconsin (LEF), and Lamont, Oklahoma (SGP). Note that LEF and SGP collect data up to 3.5 and 5 km above the ground, respectively, whereas most sites collect up to 8 km above the ground; thus, the profile extension error might be higher at these sites. Averaging over these two sites, the GOSAT $X\mathrm{CO_2}$ bias versus aircraft in this work is −0.4 ppm. The GOSAT $X\mathrm{CO_2}$ bias versus TCCON in Kulawik et al. (2016) for these two sites is −0.1 ppm. The difference between these comparisons is on the same order as the uncertainty introduced by profile extension discussed in Appendix A.

5.1.5 Predicted and actual error correlations

One surprising finding is that LMT and U actual errors are less than the predicted errors, whereas the actual $X\mathrm{CO_2}$ errors are larger than predicted, even though all three errors are calculated from the same error covariance (see Eqs. 7–8). Equation (9c) relates the errors in LMT, U, and $X\mathrm{CO_2}$. For land, an $X\mathrm{CO_2}$ error of 0.9 ppm is consistent with an LMT error of 4.6 ppm, U error of 1.8 ppm, and error correlation of −0.8. The $X\mathrm{CO_2}$ actual error (1.7 ppm) is much larger than the predicted error, whereas the LMT and U errors are smaller than predicted.

The discrepancy between the actual and predicted errors arises from the actual correlation of the LMT and U partial column mixing ratio errors. The predicted error correlation between LMT and U is −0.8. This means that values too low in LMT should be matched with values too high in U, such that the total column has lower relative errors than either partial column separately. The actual error correlation of LMT–aircraft and U–aircraft averages +0.6, meaning that when LMT is high, U also tends to be high, and $X\mathrm{CO_2}$ does not gain precision when combining LMT and U. Thus, the finding is that the LMT U error correlation must be changed from the predicted value of −0.8 to the measured value of +0.6. When the diagonal error terms are multiplied by 0.6 and the error correlation between LMT and U is set to 0.6, to match the error correlations observed versus aircraft data, the predicted LMT, U, and $X\mathrm{CO_2}$ errors are consistent with the actual errors. Over ocean, multiplying the diagonal error terms by 0.3 and setting the error correlation between LMT and U to 0.6 makes the predicted and actual errors agree.

The errors in Table 5 represent the standard deviation of GOSAT minus validation data calculated separately at each validation location. Therefore, the errors in Table 5 do not include the bias errors from Table 4. The persistent regional biases captured in the GOSAT bias variability also reflect errors in the GOSAT measurement and should somehow be combined into the full error. These regional biases likely result from persistent interferent errors, such as due to aerosols, or an interaction between spectroscopic errors and local conditions. Some but not all of the bias, particularly for LMT land,
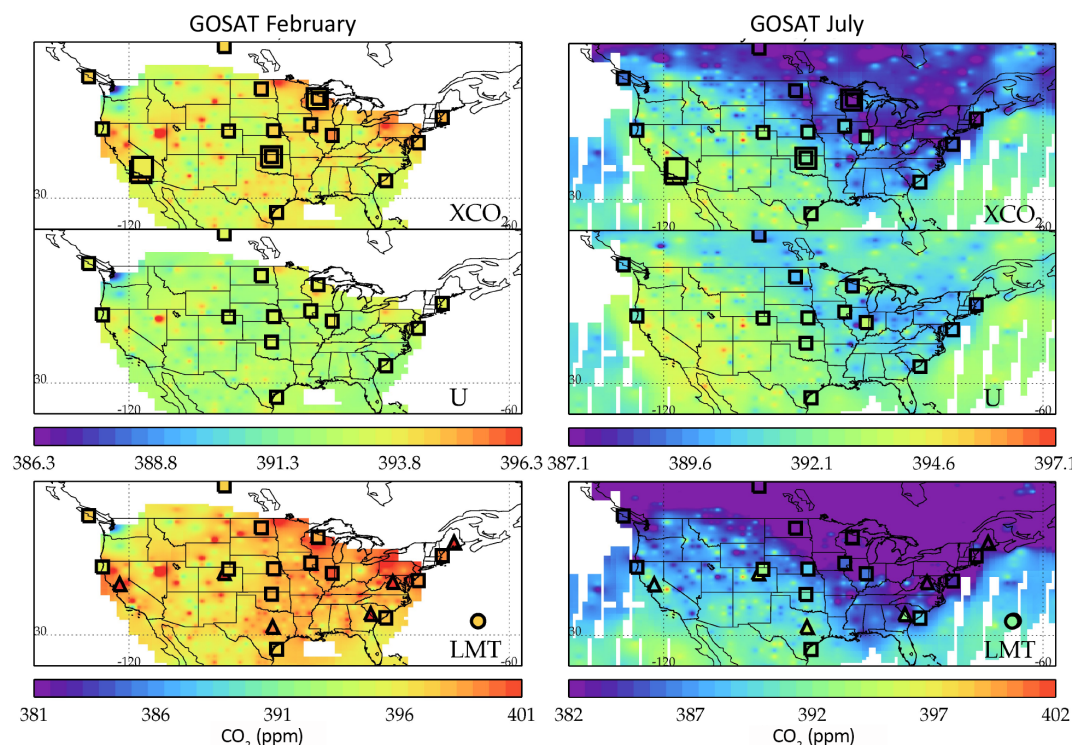
Figure 6. GOSAT XCO_2 (top), U (middle), and LMT (bottom) in February (left) and July (right). Aircraft with GOSAT averaging kernels are small squares, towers are triangles, remote ocean surface sites are circles, and TCCON are large squares (only shown on XCO_2 panels). Data are averaged over the GOSAT record.

can be attributed to colocation error (see Table 4). The correlation of the LMT and U location-dependent biases (using biases separated by location from Table B1) is also positive, 0.6, similar to the correlation of the individual errors in LMT and U. Thus, this would not account for the discrepancy between the predicted correlation of -0.8 and actual correlation of 0.6 between the LMT and U errors. Another possible reason for the positive error correlation in LMT and U is that it is a consequence of the bias correction. The error correlation on the uncorrected data was found to be -0.8, which supports that the bias correction modifies the error correlation between U and LMT. This is the first characterization of the effect of bias correction on the actual errors.

In summary, the single-sounding errors of GOSAT LMT and U over land (ocean), based on the ESRL aircraft comparison, and subtracting colocation error, are 3.4 and 1.3 ppm (1.5 and 0.8 ppm), respectively, with a positive correlation of 0.6. This is consistent with the XCO_2 error of 1.8 (1.0) ppm for land (ocean), using Eq. (9c). To find the error of averaged LMT and U, the single-sounding errors can be replaced by Eq. (11), with a and b values given in Table 6, and the same LMT U error correlation of 0.6.

5.2 Variability within the US

The CarbonTracker model identifies 19 ecoregions within North America (http://www.esrl.noaa.gov/gmd/ccgg/carbontracker/CT2011_oi/documentation_assim.html). The ESRL aircraft stations can be broadly grouped into conifer forest: PFA, ETL, ESP, THD; grass–shrub: CAR, BNE; crops: HIL, WBI, SGP; forest–field: DND, LEF, NHA, CMA, SCA; and mixed: TGC. The variability at these sites is a combination of the local activity at the site, latitude of the site, and transport into and out of the site.

Maps of GOSAT LMT, U, and XCO_2 along with aircraft, surface, tower, and TCCON observations for February and July are shown in Fig. 6 (converted to 2012 by subtracting 2 ppm per year secular increase). In February, the lower troposphere has already reached near peak values, whereas the U partial column continues to increase through April. In July, there is a large gradient in the LMT, primarily west to east, but also north to south, seen also in the stations shown in Fig. 6. The LMT pattern agrees with aircraft (Sweeney et al., 2015) and tower patterns, showing that GOSAT LMT is able to see variations in the summertime CO_2 depletion near the surface due to biospheric processes. The U partial column shows more discrepancies with aircraft than LMT, which is in general agreement, and the same pattern of discrepancies is also seen for XCO_2 versus aircraft. At the two sites where
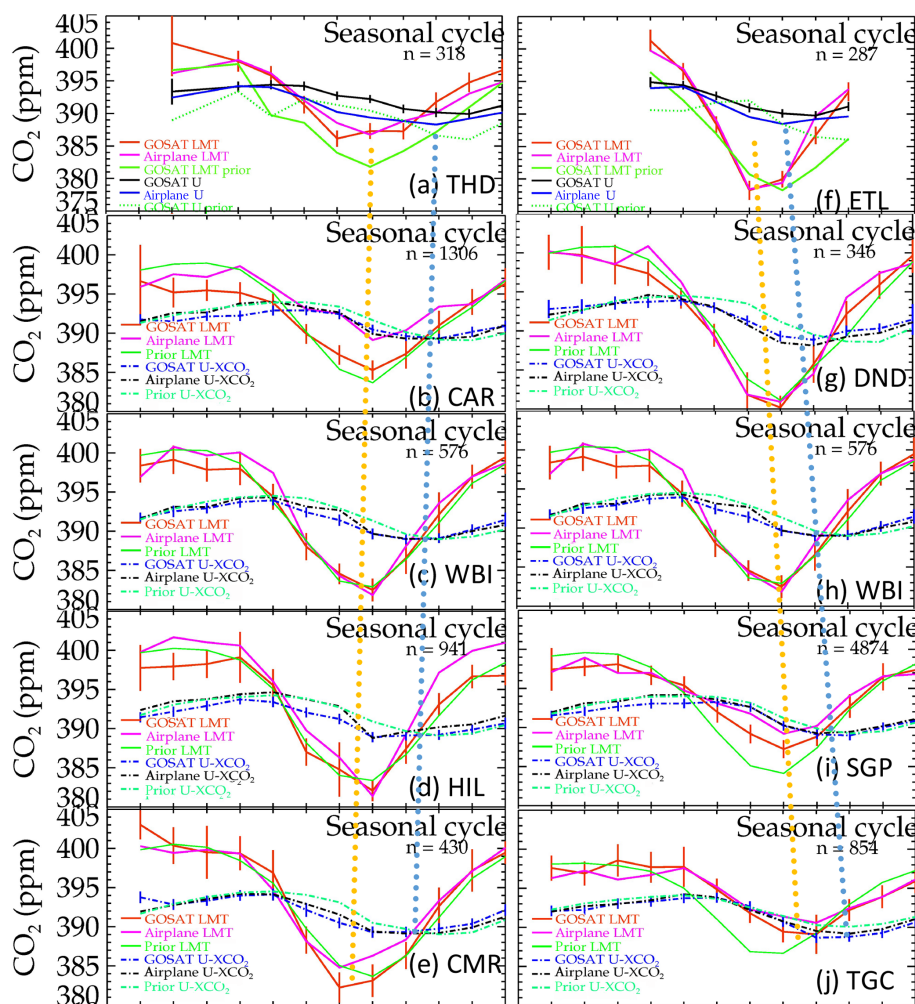
Figure 7. Seasonal cycle at five sites arranged from west to east **(a–e)** and north to south **(f–j)** for GOSAT LMT (red), aircraft LMT (pink), GOSAT LMT prior (green), GOSAT U (blue dashed), aircraft U (black dashed), and GOSAT U prior (green dashed). The seasonal cycle minimum is marked for LMT (orange dotted) and U (blue dotted).

aircraft and TCCON are jointly observed, SGP in Oklahoma and LEF in Wisconsin, XCO_2 agrees with TCCON rather than the aircraft. This suggests an issue with the extension of the aircraft profile from the top aircraft measurement (about 6 km) to the top of the atmosphere.

Figure 7 shows the seasonal cycle at five sites arranged west to east (a–e) and north to south (f–j). The seasonal cycle amplitude in LMT increases for both west-to-east and south-to-north directions. There is also a shift to later in the seasonal cycle minimum going either east to west or north to south, as seen by the slopes in the orange and blue dotted lines. There is a consistent phase lag in the U prior, e.g., the green vs. black dashed lines in panel **(c)**. The GOSAT-retrieved U improves the phase lag, e.g., see the blue dashed line in panel **(c)**. The LMT prior draw-down is also too large in panels **(i)** and **(j)**, whereas the retrieved GOSAT LMT better matches the aircraft. The seasonal cycle maximum is harder to quantify for the LMT because LMT CO_2 rises and

stays fairly flat between January and April; therefore, the maximum can be influenced by small variations in the data, in contrast to U or XCO_2, which rise steadily until April.

5.3 Comparisons to remote surface ocean sites

Remote surface sites are useful as comparisons to LMT as these locations are expected to have long vertical length scales of variability near the surface. These comparisons of LMT and remote surface ocean sites are not used for estimating errors or bias corrections because there is a mismatch in sampled vertical air mass: to compare validation data and GOSAT LMT properly, validation values are needed at every pressure level at which the GOSAT LMT averaging kernel (as seen in Fig. 3) is not zero. Since there are only validation data at the surface, the only option is to directly compare the surface site value to the GOSAT LMT result, rather than integrating validation results over the pressure range where
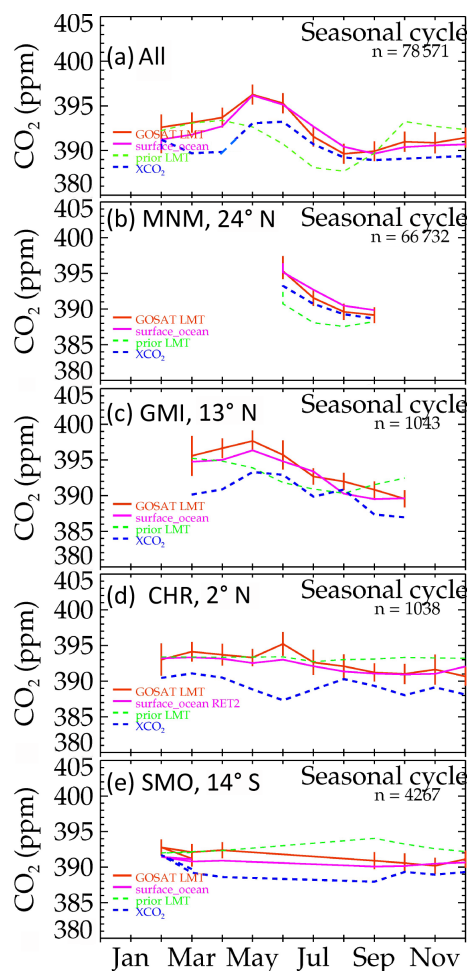
Figure 8. GOSAT LMT compared with remote ocean surface sites. GOSAT (red) improves over the prior (green dashed) versus surface sites (pink) for the average over all sites (**a**) and at the four sites with the most matches (**b–e**). XCO_2 values are shown for comparison (blue dashed).

GOSAT LMT is sensitive. The vertical colocation error is estimated by comparing CarbonTracker LMT (estimated with Eq. 6b, where x_{true} is set to the CarbonTracker value, x_a is the GOSAT prior, and cross-state error and measurement error are set to zero) versus CarbonTracker surface values. The GOSAT LMT a priori is significantly worse for remote ocean sites as compared to North America, and this allows the GOSAT product to show what is in the data versus the prior. In Table 6, the colocation error for surface ocean sites is higher than for ocean aircraft comparisons (1.0 ppm vs. 0.3 ppm, respectively), and the GOSAT bias versus ocean surface sites in Table 4 is also higher (1.1 ppm vs. 0.1 ppm, respectively). Because of the limited GOSAT ocean coverage, there are typically only about 4 consecutive months for each station, but this is adequate to evaluate the performance. Figure 8 shows an average over all locations, and the four sites with the highest number of matches, arranged from

north to south. Note the improvement of GOSAT (red) over the a priori (green) when comparing to the surface site measurements (pink). Unsurprisingly, the performance of XCO_2 (blue) shows that surface site observations are not suitable for XCO_2 validation. GOSAT LMT improves over the prior in terms of the overall bias, the bias variability, and the standard deviation over the prior even without averaging; the error reduces further with averaging.

Table 6 shows estimated colocation and correlated and random errors using Eq. (12). The colocation errors are taken from Table 4.

5.4 Source versus outflow in biomass burning with comparisons to MOPITT CO and MODIS fire counts

The southern hemispheric region is of particular interest for validation as the GOSAT prior is nearly spatially and vertically constant, varying primarily by month. Figures 9 and 10 compare GOSAT LMT and U partial column mixing ratios, respectively, to MOPITT multispectral CO retrievals and MODIS fire counts to see how much fires in this part of the world are responsible for the patterns seen in the GOSAT partial columns. The GOSAT prior, in the left columns of Figs. 9 and 10, is nearly constant in the Southern Hemisphere. The scale needed to span the seasonal range is about 13 ppm, about half that needed to capture the seasonal variability in the US.

The pattern seen in LMT matches MODIS fire count images, shown in the right column, and matches MOPITT near-surface CO shown in the third column. Because of the different overpass time and the different coverage due to cloudiness between these satellites, an exact match should not be expected. In February, sub-Saharan Africa has fires and south–central Africa does not, whereas the situation is reversed in August. This pattern is seen in GOSAT LMT, MOPITT near-surface, and MODIS fire counts. The main differences between GOSAT and MOPITT are seen in October, where GOSAT LMT shows outflow over the Atlantic and MOPITT near-surface CO does not. This may be because the multispectral CO has little surface sensitivity over the ocean.

In the mid-troposphere, MOPITT CO shows enhancement in sub-Saharan Africa in February, central Africa in August, and outflow in October, and GOSAT-retrieved U shows the same patterns as MOPITT. Interestingly, both MOPITT and GOSAT show no enhancement in South America in August, whereas the surface shows very strong enhancements in both. MOPITT shows very little outflow in September, but strong outflow in October. GOSAT does not have ocean coverage in this region for September but GOSAT U shows strong outflow in October.

The LMT signal in the Amazon region is clearly visible by May (not shown), whereas the CO signal seen from MOPITT (http://www.acom.ucar.edu/mopitt/MOPITT/data/plots6j/maps_mon.html) seems to increase starting in Au-
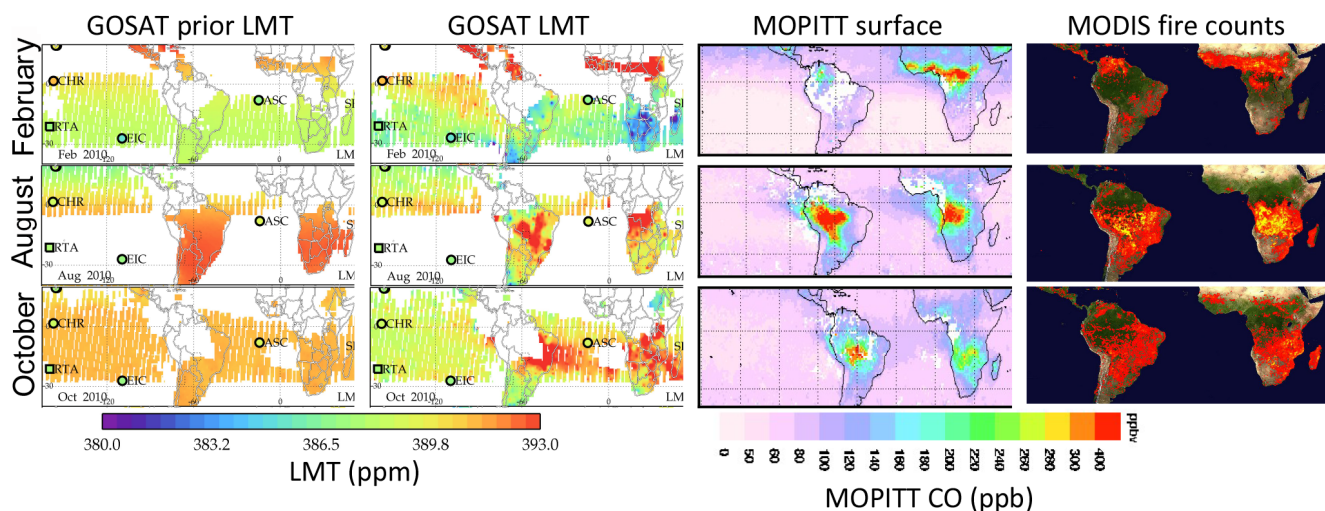
Figure 9. GOSAT LMT versus MOPITT and MODIS fire counts for February, August, and October, 2010. GOSAT prior (left) and retrieved (second column) LMT compared with MOPITT multispectral CO (third column) and MODIS fire counts (right).
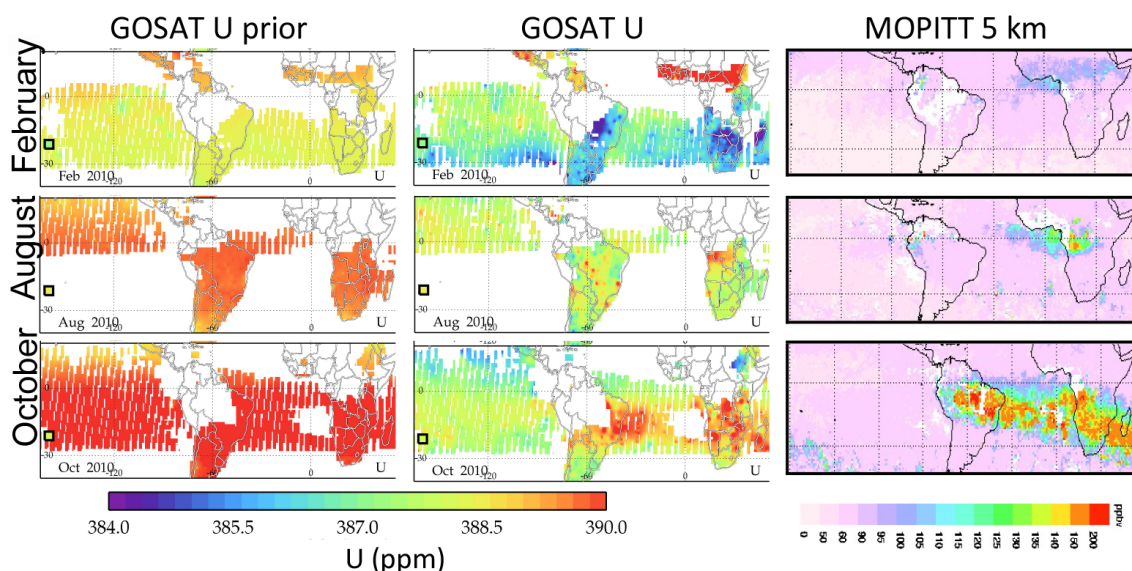

Figure 10. GOSAT U versus MOPITT for February, August, and October, 2010. GOSAT prior (left) and retrieved (middle) compared with MOPITT multispectral CO (right) at 5 km. Note the biomass burning outflow seen in October for both MOPITT and GOSAT.

gust. We look at the quantitative values for the enhancements and background values for surface CO and LMT CO_2 in Table 7 and use this to estimate $\Delta CO / \Delta CO_2$ emission ratios for May and August.

GOSAT LMT has about 0.8 DOF and does not vary significantly, mainly because only clear-sky observations (with aerosols and clouds < 0.3 optical depth) are used. The MOPITT degrees of freedom for the near-surface varies significantly. MOPITT enhancement for different degrees of freedom cutoffs are shown in different columns of Table 7. To account for the degrees of freedom, note that if a retrieved variable has 0.2 DOF, it will capture about 20 % of the true variability; if a retrieved variable has 0.4 DOF, it will capture

about 40 % of the true variability. Thus, an estimate of the emission ratio that considers the degrees of freedom is

$$\text{emission ratio} = \frac{\text{CO-CO background (ppb)}}{CO_2 - CO_2 \text{ background (ppb)}} \times \tag{14}$$
$$\frac{CO_2 \text{ degrees of freedom}}{CO \text{ degrees of freedom}}.$$

Without utilizing a model as a transfer function, the exact ratio cannot be estimated due to the varying sensitivities with altitude and different observation locations and times.

The emission ratio is estimated using Eq. (13) with the information shown in Table 7. The emission ratio estimate ranges from 6 to 7 in May and 10–15 % in August for the

Table 7. Enhancements in CO and CO_2 for May and August, 2010. The target box is 11 to 18° S, 60 to 56° W, for May and 13–17° S, 55–60° W, for August. The CO background box is 11 to 18° S, 40 to 44° W, for May and 157.8–161.8° W, 19–23° S, for August. Rarotonga aircraft measurements are used for CO_2 background. The different CO target columns are for different cutoffs for the degrees of freedom between the surface and 200 hPa above the surface for MOPITT.

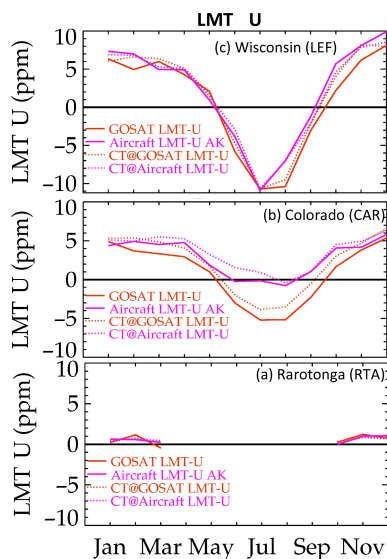|		CO					GOSAT LMT CO_2	
		Background (ppb)	Target all (ppb)	Target DOF > 0.15) (ppb)	Target (DOF > 0.25) (ppb)	Target (DOF > 0.30) (ppb)	Background from RTA (ppm)	Target (DOF = 0.8) (ppm)
May 2010	Mean	68 ± 9	122 ± 49	123 ± 54	146 ± 77	182 ± 96	386.4	389.6 ± 2.5
	N	1502	2023	1556	500	215		26
	DOF		0.21	0.24	0.32	0.39		0.85
	Δ value	–	54	55	88	114	–	3.2
	Em. ratio		6 %	6 %	7 %	7 %	–	–
August 2010	Mean	91 ± 22	305 ± 171	311 ± 180	336 ± 200	372 ± 221	387.4	393.1 ± 4.8
	N	2989	3881	3227	1887	1231		49
	Δ value (ppb)	–	213.7	219.3	244.8	281.1	–	5.7
	Em. ratio		15 %	13 %	11 %	10 %		

Figure 11. GOSAT LMT – U (red) versus aircraft (pink) at three sites. The dotted lines show CarbonTracker matched to GOSAT (red dotted) or aircraft (pink dotted). Colocation error explains the discrepancies in the drawdown at CAR and LEF. At CAR the discrepancies are due to mismatch at the time of day the data are collected.

different MOPITT sensitivity groupings. The emission ratio seen by the MOPITT and GOSAT LMT products are compared to those estimated from aircraft observations over tropical forests by Akagi et al. (2011, Table 1), which is 8.8 %. The MOPITT / GOSAT ratio is similar to Akagi et al. (2011), but 2–3 lower in May and 1–6 % higher in August.

5.5 Differences between LMT and U

The difference between CO_2 in the free troposphere and boundary layer can be used to evaluate model transport. One previous finding is that surface assimilation estimates of northern extratropical and southern hemispheric land flux differences are correlated with the gradients between CO_2 at 4 and 1 km in the assimilated model. When the model-based vertical gradients of CO_2 are larger than aircraft observations, models tend to predict too-large northern hemispheric sinks and too-large southern hemispheric sources (Stephens et al., 2007). Aircraft observations of CO_2 at 4 and 1 km are taken at only a few sites worldwide, primarily in the US. Therefore, global measurements of the difference between CO_2 in the free troposphere and boundary layer are of great interest. In this section we calculate the errors for LMT U compared to aircraft profiles and show this difference for GOSAT and CarbonTracker in the US and the Southern Hemisphere in 2 different months.

The error estimate for LMT U is calculated using Eq. (14). Note that a positive correlation in the errors for LMT and U results in a smaller error for the quantity (LMT – U) than the sum of the squares of LMT and U.

$$\sigma_{(LMT-U)} = \sqrt{\sigma_{lmt}^2 + \sigma_u^2 - 2 \cdot \sigma_{lmt}\sigma_u c} \tag{15}$$

Table 8a–c give the bias, standard deviation, and error with averaging for LMT – U. In Table 8a, the GOSAT bias and bias variability of (LMT – U) improves over the prior for all cases. The bias variability of 0.3, 0.9, and 0.8 ppm of (LMT – U) for HIPPO ocean, ESRL ocean, and ESRL land, respectively, is comparable to the LMT bias variability of 0.3, 1.0, and 1.0 for the same categories. In Table 8b, the 15-observation average standard deviation for GOSAT LMT U is 0.6 (1.2) ppm for ocean (land), 0.2 ppm higher for ocean,
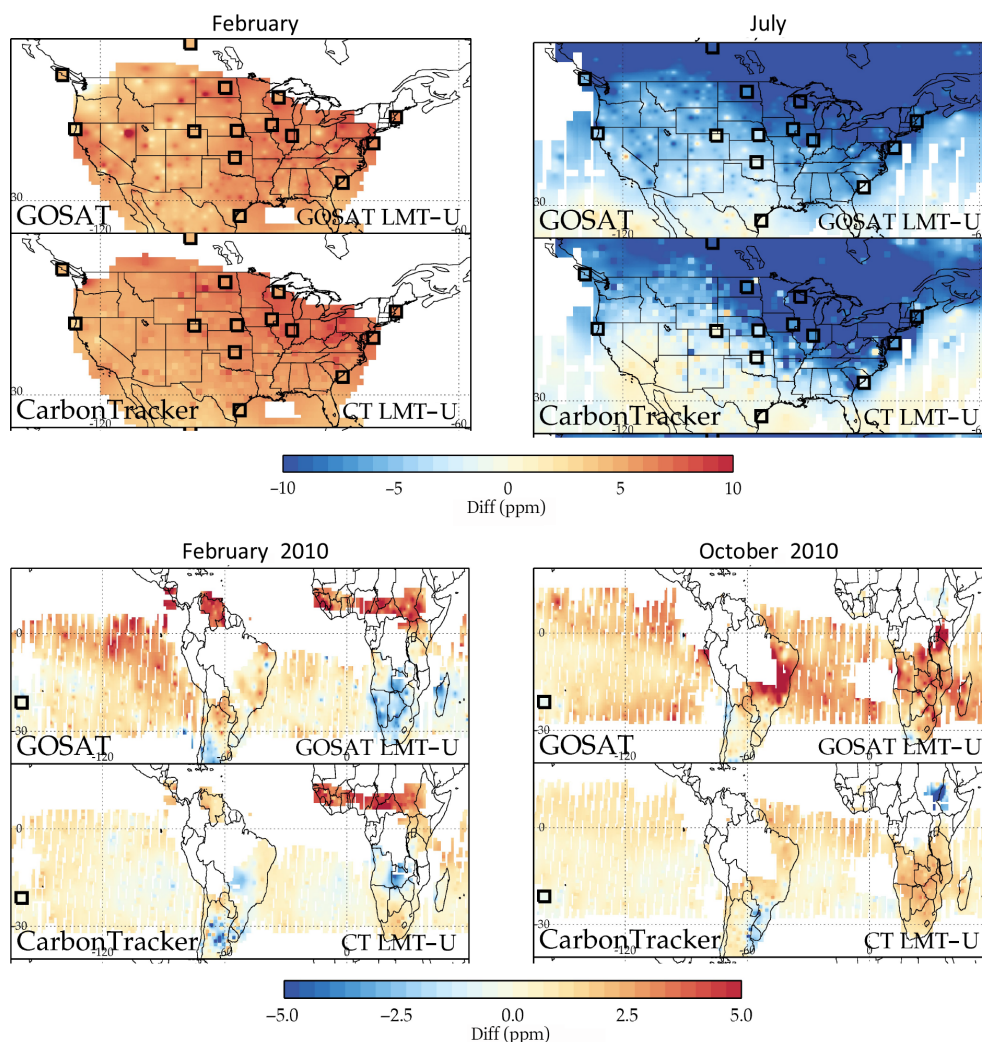
Figure 12. LMT – U differences. Results shown for the US (top) and South America and Africa (bottom) for 2 different months, with GOSAT on the top and CarbonTracker on the bottom. Aircraft LMT – U differences are shown in the squares. There is agreement in the US, except for the southwestern US in July, with more differences in the Southern Hemisphere.

and 0.7 ppm lower for land than LMT. In Table 8c, the correlated error is 0.5 (0.9) ppm for ocean (land), which is 0.2 ppm higher for ocean and 0.8 ppm lower for land. The land standard deviation for LMT U is 2.3 ppm before subtracting off the 2.1 ppm colocation error. The difference between the land error for LMT and LMT U is due to the estimated size of the colocation error.

Figure 11 shows the seasonal cycle of LMT U for three sites. The differences between GOSAT and aircraft values at the CAR site in Colorado and LEF in Wisconsin during the drawdown can be explained by colocation error. The dotted lines show CarbonTracker matched to GOSAT (red dotted) or aircraft (pink dotted) locations and times. The difference between the red dotted and pink dotted lines estimate the colocation error. If GOSAT were corrected by this difference, the agreement with aircraft would be much better. The colocation bias and standard deviation are estimated in Table 7a and

7b and are large compared to the observed GOSAT errors. The error estimates for GOSAT are corrected by the colocation error. Note that the CAR aircraft measurements also did not sample down to the boundary layer during this time period.

The predicted error for LMT U over land in Table 8b is 2.7 ppm, whereas the actual error is 2.3 ppm. If LMT and U had zero correlation, the predicted error (using Eq. 14) would be 3.6 ppm. This is another corroboration of the positive correlation between the LMT and U errors.

Figure 12 shows LMT – U for February and July in the US, averaged over 2010–2014 for February and 2009–2013 for July. LMT – U diagnoses model vertical transport (Stephens, 2007) and transport of outflow (Deeter, 2013). Aircraft values for LMT – U are shown as squares. The aircraft patterns are captured by GOSAT, with discrepancies in July for BNE, CAR, SCA, and SGP due to colocation error

Table 8. (a) Bias terms for LMT − U. Compare to Table 4. **(b)** Standard deviations for LMT − U. Compare to Table 5. The predicted errors in the table use the errors given at the end of Sect. 5.1.5. **(c)** Error fits for LMT − U. Compare to Table 6.

(a)	HIPPO ocean (ppm)	ESRL ocean (ppm)	ESRL land (ppm)
Colocation bias	-0.4 ± 0.2	-0.2 ± 0.3	$--0.6 \pm 0.5$
True mean	1.1 ± 0.8	0.4 ± 0.5	1.0 ± 2.7
Prior bias	-1.0 ± 1.3	-2.8 ± 2.9	-1.0 ± 1.2
GOSAT bias	0.0 ± 0.4	-0.5 ± 0.9	-0.5 ± 0.8
(b)			
Colocation error	0.3 ± 0.1	0.3 ± 0.1	2.1 ± 0.7
Predicted error ($n = 1$)	1.2 ± 0.0	1.2 ± 0.0	2.7 ± 0.0
GOSAT error ($n = 1$)	1.5 ± 0.4	1.3 ± 0.1	2.3 ± 0.5
True variability	0.5 ± 0.2	0.8 ± 0.1	4.8 ± 1.5
Prior error ($n = 15$)	0.5 ± 0.2	0.8 ± 0.1	1.4 ± 0.8
GOSAT error ($n = 15$)	0.5 ± 0.2	0.7 ± 0.1	1.2 ± 0.8
(c)			
Colocation error	0.3 ± 0.1	0.3 ± 0.1	2.1 ± 0.7
Correlated error (a)	0.4 ± 0.2	0.6 ± 0.0	0.9 ± 0.9
Random error (b)	1.4 ± 0.4	1.1 ± 0.1	2.1 ± 0.7

(see CAR plot in Fig. 11). The CarbonTracker model captures the aircraft patterns very well. The main differences between GOSAT and CarbonTracker are seen in the southwestern US in July (where there are no aircraft measurements). Figure 12c–d show LMT − U for February and October in the Southern Hemisphere. The only aircraft site in this region is Rarotonga, where Fig. 11 shows good agreement for both CarbonTracker and GOSAT. The patterns in the Southern Hemisphere show more differences between CarbonTracker and GOSAT. In February, GOSAT shows a high gradient in the eastern Pacific and northern South America, which is not seen in CarbonTracker, and it shows a more negative gradient in central and southern Africa. In October large gradients are seen by GOSAT in South America and Africa with outflow into the Atlantic, with little seen in CarbonTracker.

LMT U is predominantly positive in this southern hemispheric region in October. Vertical transport from the Northern Hemisphere would predominantly show up in the U partial column, whereas flux from land or ocean would predominantly show up in the LMT partial column. An overall positive value for LMT − U could either suggest that the overall flux is positive in this month or that transport from the Northern Hemisphere was negative, though the blank space in the Amazon due to cloudy conditions, where LMT U is expected to be negative from plant uptake, creates uncertainty both in this crude estimate and in the formal assimilated results from GOSAT data.

6 Discussion and conclusions

GOSAT near-infrared observations provide information to retrieve two partial column mixing ratios, one from the surface to about 2.5 km (LMT_XCO$_2$) and the second above about 2.5 km (U_XCO$_2$). The two partial columns have distinct seasonal cycles, with the LMT peaks and troughs earlier than XCO$_2$, and the U peaks and troughs later than XCO$_2$, with the partial columns showing similar patterns to those observed from the NOAA aircraft (e.g., Sweeney et al., 2015). After bias correction, shown in detail in Appendix A, and following the same process as the bias correction for ACOS-GOSAT XCO$_2$, both partial column mixing ratios show agreement with aircraft, LMT shows agreement with remote surface observations, and both show improvement over the GOSAT prior. Single observations for land have observation errors of 3.4, 1.3, and 1.7 ppm for LMT, U, and XCO$_2$, respectively, and single observations for ocean have observation errors of 1.5, 0.8, and 0.9 ppm for LMT, U, and XCO$_2$, respectively. These errors are significantly reduced with averaging, though some systematic errors, generally below 1 ppm, remain. The colocation errors from mismatch of GOSAT versus validation data, as quantified by CarbonTracker, makes the errors on LMT challenging to validate, and extension of validation data to the top of the atmosphere with modeled CO2 adds uncertainty on the order of 0.4 ppm to the LMT bias. The value of observing two partial columns can be seen in Fig. 8, where the GOSAT LMT agrees with remote surface sites, whereas neither the prior nor XCO$_2$ agree with the surface site, and Figs. 9–10, where surface versus

tropospheric CO_2 are distinguished for source and outflow of African biomass burning emissions in August and October. The observed LMT CO_2 enhancements with MOPITT multispectral CO and emission ratios are compared to Akagi et al. (2011), with our emission ratio 2–3 lower in May and 1–6 % higher in August. The LMT minus U difference, which can be used to evaluate model transport error (e.g., Stephens et al., 2007), has also been evaluated with monthly average error of 0.8 (1.4) ppm for ocean (land). The new LMT partial column mixing ratio allows the local boundary air to be distinguished from the free troposphere and captured in the U partial column mixing ratio, and it better disentangles local versus remotely influenced signals.

Appendix A: Bias correction

The ACOS-GOSAT XCO_2 product undergoes bias correction (Wunch et al., 2011), which significantly improves the errors (Kulawik, 2016). We apply this same technique to correct the LMT product. Land nadir mode (land) and ocean glint mode (ocean) are bias corrected separately for LMT. Following the LMT correction, U is corrected by subtracting the LMT partial column from XCO_2 corrected for ACOS-GOSAT, thus maintaining consistency between the $[LMT, U]$ partial columns and the total XCO_2 column after bias correction. This is done because the XCO_2 bias correction has been checked against TCCON, which has sensitivity throughout the entire column, and because there is uncertainty in the true U used for validation, which is calculated from aircraft extended with the CarbonTracker model above about 5 km, composing a large part of the U partial column.

To determine the LMT bias correction, GOSAT and aircraft data are matched using dynamic coincidence criteria (Wunch, 2011), and the difference between GOSAT LMT and aircraft LMT is calculated for all pairs in either land or ocean groups versus each potential parameter. In order to identify the critical bias-predicting parameters for those cases for which this difference has a clear slope, a bias correction is applied iteratively, where the strongest parameter dependence is corrected before the next parameters are tested. At the end all parameters are fit simultaneously. Filters are applied to flag the data as bad when the bias is significant even after correction. The parameters considered for bias correction are: delta_grad_co2, albedo_1, albedo_2, albedo_3, albedo_ slope_1, albedo_slope_2, albedo_slope_3, aod_dust, aod_ice, aod_total, b1offset, ice_height, surfacePressure_xa, surfacePressureDiff, co2_ratio, dp_cld, h2o_ratio, s32, xco2_error, LMT_ dofs (degrees of freedom for LMT), u_dofs (degrees of freedom for U), xco2_dofs, asza, lza, and delta_ grad_co2_prime. These parameters are described in the ACOS-GOSAT v3.5 user's guide, with the exception of delta_grad_co2_prime, which is defined as delta_grad_co2 with the value set to 50 when it is greater than 50 for land and the value set to -10 when it is greater than -10 for ocean. Two figures of merit were considered for the cutoffs and bias fits, (1) bias variability by location and season and (2) the single-observation standard deviation. The former is the standard deviation of the biases calculated in four seasons and for each location and campaign. For both of these figures of merit, smaller is better.

By far the strongest bias is related to delta_grad_CO2. This parameter is the difference between the retrieved CO_2 and a priori dry-air mole fraction between the surface and vertical level 13 (approximately 630 hPa for soundings near sea level), and it represents the slope of the retrieved CO_2 profile in the troposphere. The resulting coefficient for this term is 0.396 for ocean and 0.310 for land soundings. This indicates that, for ocean, approximately 40 % of the CO_2 at-

tributed to the surface should be moved from LMT to U. This indicates that possibly (a) the troposphere is constrained too much relative to the surface, (b) there is an issue with the forward model, such as systematic errors in spectroscopy, or (c) there is some other retrieval artefact. The bias correction coefficient for delta_grad_CO2 for simulated OCO-2 land data is 0.29, very similar to the value of 0.31 for actual GOSAT data (Kulawik, unpublished result). The simulated runs have no spectroscopic error or other forward model errors; thus, the need for delta_grad_CO2 correction is likely not driven by forward model errors but could be a consequence of the way the CO_2 profile is constrained in the retrieval through the constraint matrix, which allows a lot of variability near the surface and damps variability in the midtroposphere. This could prejudice the retrieval system to attribute radiance variations to CO_2 variations at the surface rather than elsewhere in the profile, with the delta_grad_CO2 correction factor undoing this tendency. This relationship should be explored further using a simulated system with different constraint matrices.

The filtering cutoffs and bias terms are shown in Table A1. The errors are calculated by the bootstrap method (Rubin, 1981). The effects of the cutoffs and bias corrections from Table A1 on biases and standard deviations are shown in Table A2.

The overall land bias is not zero because the land bias constant correction undergoes a final step to harmonize land and ocean observations by matching GOSAT values for pairs of close land and ocean observations. The results (using the final bias correction) for different matching criteria are 1° and 1 h (25 matches, bias -0.54 ppm in LMT and -0.96 ppm in XCO_2), 2° and 24 h (295 matches, 0.17 ppm in LMT and -0.61 ppm in XCO_2), 4° and 48 h (4095 matches, 1.17 ppm in LMT and -0.09 ppm in XCO_2), and with dynamic coincidence criteria (422,542 matches, 0.29 ppm in LMT, -0.42 in XCO_2). Using the assumption that there is no bias in XCO_2, the 4°, 48 h result is used, and 1.17 ppm is added to the LMT constant bias for land. This constant bias is subtracted from LMT, and then the LMT partial column is subtracted from XCO_2 to generate the corrected U partial column. The 1.2 ppm change in the land bias to match ocean results gives an idea of the size of the uncertainty in the bias.

As seen from Table A3a and b, all bias corrections are superior to the uncorrected dataset, and all correction tests perform similarly in the bias standard deviation and mean standard deviation, but with variability in the overall bias, depending on the development set that is used. The overall bias has some uncertainty on the order of 0.5 ppm.

Another potential error source that is quantified is the effect of different profile extension schemes above aircraft observations. The ESRL aircraft measurements go up to 5–8 km aboveground, and the HIPPO observations go up to 9–13 km aboveground. Four different profile extension methods are tried above the aircraft: (1) using the GOSAT a priori profile, (2) extending the top aircraft measurement to the

Table A1. Filtering and bias corrections. Note that observations over land and ocean are corrected separately.

Parameter	Ocean filtering	Ocean bias correction	Land filtering	Land bias correction
albedo_2	$0.0215 < \text{val} < 0.024$	-1272.02 ± 50	–	–
albedo_slope_2	$\text{val} < 8e\text{-}6$	–	–	–
aod_dust	$\text{val} < 0.01$	–	–	-36.03 ± 1
aod_total	$\text{val} < 0.25$	–	–	–
h2o_ratio	$0.96 < \text{val} < 1.02$	–	–	–
co2_grad_delta	$-40 < \text{val} < 17$	0.396330 ± 0.004	–	0.310 ± 0.003
constant	–	52.674 ± 6	–	0.01259 ± 0.4
b1_offset	–	-1.2520 ± 0.05	–	–
surfacepressure_xa	–	-0.0381105 ± 0.006	–	–
s32	–	17.0742 ± 3	–	–
surfacepressurediff	–	0.869280 ± 0.05	–	–
albedo_1	–	144.458 ± 9	–	–
co2_grad_delta_prime	–	-0.171350 ± 0.01	–	-0.027 ± 0.005
dofs_LMT	–	–	$\text{val} > 0.68$	–
xco2_error	–	–	$\text{val} < 1.4$	6.02 ± 0.3
albedo_slope_3	–	–	$-1.5 \times 10^{-4} < \text{val} < 2.0 \times 10^{-4}$	–
xco2_dofs	–	–	$\text{val} > 1.3$	–
ice_height	–	–	$\text{val} > -0.1$	–
surfacePressureDiff	–	–	$-4 < \text{val} < 2$	–
albedo_3	–	–	–	-11.66 ± 0.7
dp_cld	–	–	–	0.219 ± 0.01

* Parameters also used in ACOS-GOSAT XCO_2 bias correction.

Table A2. (a) Effects of bias corrections and quality flags on land comparisons (ESRL aircraft land observations). **(b)** Effects of bias corrections and quality flags on ocean comparisons (HIPPO and ESLR ocean dataset stations and campaigns: tgc, rta, aoa, 2S, 2N, 3S, 3N, 4S, 4N, 5S, 5N).

	n	lmt bias (ppm)	lmt bias var. (ppm)	lmt stdev (ppm)	u bias var. (ppm)	u stdev (ppm)
(a)						
Original (XCO_2 flags)	15143	13.54	2.79	7.70	1.61	3.05
All quality flags (see Appendix A)	12714	13.37	2.30	7.55	1.27	2.98
Bias correction (see Appendix A)	12714	-1.18	1.43	3.47	0.79	1.36
Fit U separately	11978	–	–	–	0.70	1.43
(b)						
Original (XCO_2 flags)	9836	1.73	3.46	3.77	0.78	0.85
With cutoffs (see Appendix A)	6143	1.47	1.92	3.18	0.63	0.69
Bias correction (see Appendix A)	6143	0.04	0.68	1.60	0.38	0.79
Fit U separately	6143	–	–	–	0.35	0.60

The fit parameters are tested for robustness by using a subset of the dataset to determine the fit and then testing the fit on the independent subset. For the ocean data, HIPPO campaigns 2N, 3S, 4, and 5 are used to develop bias correction, and HIPPO 2S and 3N are used for testing. For land data, stations bne, car, cma, dnd, esp, etl, hil, and hip are used for development, and stations lef, nha, pfa, sca, sgp, tgc, thd, and wbi are used for testing.

tropopause pressure with the GOSAT prior above this, (3) using the CT2015 model, and (4) extending the top aircraft measurement to the tropopause pressure with the CT2015 model above this. Table A4 shows the land and ocean characteristics with each profile extension type. The main effect is on the overall bias (up to 0.4 ppm) in the comparisons. One issue is likely in the top 4 levels, from which a difference

between a priori and the true profile would propagate as a bias.

Table A5 compares the extension with AirCore versus CarbonTracker. AirCore measures from the surface up to as high as 13 hPa, meaning that all but the top GOSAT pressure level is measured. Eight AirCore observations are found to match aircraft and GOSAT observations within 3° longitude, 5° lat-

Table A3. (a) Bias correction robustness test for LMT observations over ocean. Comparisons to aircraft data are tested using (1) no bias correction, (2) bias correction using the test dataset, (3) an independent dataset, and (4) the entire dataset. **(b)** Bias correction robustness test for LMT observations over land. Same as Table A3a but for land.

(a)

Bias correction testing	Mean bias	Bias SD	mean SD
No correction	0.69	0.69	2.97
Subset tested on itself	−0.04	0.33	1.47
Independent subset	−0.26	0.46	1.58
All data used	−0.14	0.49	1.54

(b)

No correction	13.00	2.47	7.54
Subset tested on itself	0.16	1.55	3.68
Independent subset	1.05	1.24	3.67
All data used	0.50	1.51	3.65

itude, and 7 days. Six of the matches are at SGP and two are at CAR. For these matches, the aircraft observations are extended either with AirCore (using CarbonTracker at only the top pressure level) or CarbonTracker. The finding is similar to the finding from Table A4 that there is uncertainty in the overall bias of 0.4 ppm, but that the standard deviation is not affected by which extension is used. The reason for the 0.4 ppm bias is that the CarbonTracker stratosphere is high compared to AirCore for these eight observations. This propagates into a high bias in the true U and a low bias in the true LMT through the averaging kernel. Because there is uncertainty in the true value of the stratosphere that is used to extend the aircraft profiles, there is some uncertainty in the overall bias of GOSAT LMT and U on the order of 0.4 ppm.

Table A5. Effect of profile extension, part 2. Extension of the aircraft with CarbonTracker versus extension with AirCore.

Profile extension	LMT bias	LMT SD	U bias	U SD
(a) CT2015	0.3	3.1	−0.2	1.0
(b) AirCore	0.0	3.1	0.2	1.0

There were several ways that the developed bias correction was insulated from the validation: (1) the bias correction uses dynamic coincidence criteria (Wunch, 2011), whereas the comparisons to validation data use geometric coincidence criteria ($\pm 5°$ latitude and longitude, and ± 1 week). The overlap between these two sets is about 50 %. (2) Remote ocean surface sites were not used to develop the bias correction. These locations are expected to have good mixing between the surface and 2.5 km, but since we do not have profiles at these locations, these observations are not used for direct validation. These comparisons between GOSAT and remote surface sites show excellent improvement over the GOSAT prior. (3) No data over the southern hemispheric biomass burning are used in the bias correction, and GOSAT compares very well to MOPITT in this region. (4) Comparisons were made, taking out observations used in the bias correction at SGP, where there are plenty of matches. These comparisons were as good as the full set.

The mean and standard deviation of the bias correction is -11.4 ± 7.6 and 2.7 ± 2.7 ppm for LMT and U land, respectively and -1.0 ± 3.1 and -1.7 ± 0.9 ppm for LMT and U ocean, respectively. The mean and standard deviations of the bias correction for XCO$_2$ are -0.6 ± 1.0 ppm for land and -0.6 ± 0.6 for ocean. The bias corrections are larger for the partial columns than for XCO$_2$; the size and variability of the bias correction is an indication of its importance.

Table A4. Effect of profile extension. GOSAT corrected as described in Table A1 and compared to aircraft data with profile extended four different ways: (a) using the GOSAT prior, (b) extending the aircraft to the tropopause pressure, with the GOSAT prior above this, (c) using the CT2015 model, and (d) extending the aircraft to the tropopause pressure, with the CT2015 above this.

Profile extension	LMT bias	LMT Bias SD	LMT SD	U bias	U Bias SD	U SD
(a) prior	−0.90	1.37	3.46	−0.38	0.70	1.25
(b) extend + prior	−0.99	1.44	3.47	−0.20	0.79	1.35
(c) CT2015	−1.20	1.39	3.47	−0.02	0.66	1.26
(d) extend + CT2015	−1.18	1.43	3.47	−0.05	0.79	1.36

Appendix B: Detailed comparisons by site and campaign

In addition to the averaged results provided previously, Table B1 below breaks down the validation results for each individual station. This table could be useful for diagnosing outliers in the comparisons, looking at correlations of site-to-site biases or standard deviations in LMT and U.

Table B1. Actual and predictions of errors by station and campaign. See Table 3 for definitions of the quantities calculated in Table B1.

Location	Latitude, longitude	Colocation error (ppm)	a corr. error (ppm)	b rand. error (ppm)	GOSAT prior bias ($n=1$) (ppm)	GOSAT error ($n=1$) (ppm)	Pred. error ($n=1$) (ppm)	Colocation bias (ppm)	True mean (ppm)	Prior bias (ppm)	GOSAT bias (ppm)	True stdev ($n=1$) (ppm)	Prior error ($n=15$) (ppm)	GOSAT error ($n=15$) (ppm)
						(a) LMT vs. surface ocean flasks at remote sites								
BMW	32° N, 65° W	0.4	0.9	2.5	4.6	2.6	4.2	−0.8	391.8	−3.0	−1.4	3.3	2.8	1.1
MID	28° N, 177° W	0.8	1.5	1.8	4.2	2.3	4.3	0.1	389.9	−2.4	−0.2	2.2	4.5	1.5
MNM	24° N, 154° E	0.3	0.8	1.6	3.8	1.8	4.2	0.2	393.2	−3.8	−0.6	1.6	2.8	0.9
MLO	20° N, 156° W	0.8	1.0	1.4	2.6	1.7	4.5	−0.6	390.9	−2.1	−0.3	1.7	2.2	1.0
KUM	20° N, 15° 5W	0.7	1.5	1.2	2.6	1.9	4.5	−0.6	390.0	−1.1	0.7	1.7	2.5	1.5
GMI	13° N, 145° E	0.5	0.7	1.6	2.8	1.8	4.4	0.0	394.8	−2.9	0.9	1.2	1.9	0.8
CHR	2° N, 157° W	0.3	0.8	1.4	1.6	1.6	4.4	−0.2	392.1	−0.8	0.4	1.1	1.9	0.9
SEY	5° S, 56° E	0.4	1.3	1.8	2.2	2.2	4.0	−0.3	391.4	−0.2	0.7	1.3	0.8	1.3
ASC	8° S, 14° W	0.3	1.0	1.5	1.7	1.8	4.4	−0.4	390.4	0.1	1.5	0.7	2.5	1.1
SMO	14° S, 171° W	0.5	0.5	1.7	2.2	1.8	4.2	−0.5	390.6	0.0	0.6	0.5	2.2	0.7
EIC	27° S, 109° W	0.5	0.8	1.2	2.1	1.4	4.2	−0.4	389.7	0.7	2.7	0.7	1.9	0.8
	Average	0.5 ± 0.2	1.0 ± 0.3	1.5 ± 0.2	2.6 ± 0.8	1.8 ± 0.3	4.3 ± 0.2	−0.3 ± 0.3	391.3 ± 1.6	−1.2 ± 1.5	0.7 ± 1.0	1.3 ± 0.5	2.3 ± 0.9	1.1 ± 0.3
						(b) LMT vs. ESRL aircraft								
PFA	66° N, 147° W	1.6	5.0	1.6	2.1	5.3	5.1	0.1	388.0	1.9	0.3	8.2	1.5	5.0
ETL	54° N, 105° W	2.2	2.6	2.6	3.6	3.7	4.8	−0.3	388.7	−1.0	−0.6	6.9	3.5	2.7
ESP	49° N, 126° W	3.2	3.2	4.6	4.1	5.6	5.0	0.0	386.1	−2.4	−0.2	4.4	3.6	3.4
DND	47° N, 99° W	1.4	2.9	2.4	3.8	3.8	4.5	−0.1	390.0	−0.6	−0.7	7.8	5.0	3.0
LEF	46° N, 90° W	2.6	3.5	2.2	3.7	4.1	4.7	−0.3	392.1	−0.9	−1.4	6.8	4.5	3.5
NHA	43° N, 71° W	1.6	1.9	3.5	2.8	4.0	4.8	−0.3	393.3	−0.1	0.1	7.7	2.6	2.1
WBI	42° N, 91° W	2.8	1.9	2.9	2.6	3.5	4.5	−1.5	393.3	−0.7	−0.9	5.1	2.3	2.1
THD	41° N, 124° W	2.2	2.7	3.5	2.5	4.4	4.6	0.3	389.5	−1.5	0.9	3.9	2.5	2.8
BNE	41° N, 97° W	2.1	2.4	3.0	3.3	3.9	4.4	−1.3	393.2	−2.5	−2.2	5.0	3.1	2.5
CAR	41° N, 104° W	2.7	2.7	3.3	3.6	4.2	4.2	−2.2	393.0	−2.7	−2.6	3.5	3.3	2.8
HIL	40° N, 88° W	2.2	2.2	3.0	3.4	3.8	4.5	−0.9	396.3	−2.0	−2.4	5.7	3.1	2.4
CMA	39° N, 74° W	1.8	1.8	3.7	3.0	4.1	4.8	−0.6	394.9	−0.7	−0.5	6.1	2.3	2.0
SGP	37° N, 98° W	1.8	2.7	2.9	4.1	3.9	4.3	−0.5	394.3	−1.5	−0.7	4.2	3.7	2.8
SCA	33° N, 79° W	1.0	1.1	3.2	2.3	3.3	4.8	−0.5	395.6	0.3	−1.3	2.9	1.8	1.3
AOA	29° N, 148° E	0.4	0.7	1.2	1.1	1.4	4.2	−0.5	392.4	−5.0	−0.8	1.5	0.9	0.8
TGC	28° N, 97° W	1.1	1.5	2.5	2.7	2.9	4.2	−0.1	394.9	−0.2	0.0	2.7	2.3	1.7
RTA	21° S, 160° W	0.4	0.2	1.6	1.0	1.6	4.3	0.0	390.9	1.3	0.7	0.7	0.7	0.5
	Average land	2.0 ± 0.6	2.5 ± 1.2	3.0 ± 0.7	3.2 ± 0.6	4.0 ± 0.7	4.6 ± 0.3	−0.5 ± 0.7	392.2 ± 3.1	−1.0 ± 1.2	−0.8 ± 1.0	5.4 ± 1.8	3.0 ± 1.0	2.7 ± 0.9
	Ave. land, corrected		1.5 ± 1.2		2.4 ± 0.6	3.4 ± 0.7				−0.5 ± 01.2	−0.3 ± 1.0		2.2 ± 1.0	1.7 ± 0.9
AOA, RTA	Average ocean	0.4 ± 0.0	0.4 ± 0.5	1.4 ± 0.3	1.1 ± 0.1	1.5 ± 0.1	4.3 ± 0.1	−0.3 ± 0.4	391.7 ± 1.1	−1.9 ± 04.5	−0.1 ± 1.1	1.1 ± 0.6	0.8 ± 0.1	0.7 ± 0.2
						(c) U vs. ESRL aircraft								
PFA	66° N, 147° W	0.5	1.3	1.1	1.3	1.7	1.8	0.1	392.0	1.8	1.5	2.4	1.0	1.3
ETL	54° N, 105° W	0.4	1.0	1.2	1.6	1.6	1.8	0.1	390.8	1.3	0.9	1.8	1.7	1.1
ESP	49° N, 126° W	1.2	2.0	1.1	1.6	2.3	1.8	0.4	389.9	1.7	2.2	2.1	1.9	2.0
DND	47° N, 99° W	0.6	0.7	1.3	1.6	1.5	1.8	0.2	390.5	0.8	0.4	2.2	1.8	0.8
LEF	46° N, 90° W	0.5	0.5	1.2	1.4	1.3	1.8	0.0	391.3	0.4	0.1	2.1	1.5	0.6
NHA	43° N, 71° W	0.5	0.8	1.2	1.3	1.5	1.8	0.0	391.5	0.4	0.3	2.5	0.9	0.8
WBI	42° N, 91° W	0.4	0.6	1.1	0.8	1.2	1.8	−0.2	391.2	0.3	−0.2	2.1	0.6	0.7
THD	41° N, 124° W	0.9	1.0	1.2	1.2	1.6	1.8	0.4	390.5	1.4	1.8	1.9	0.8	1.1
BNE	41° N, 97° W	0.4	0.6	1.2	1.1	1.3	1.7	−0.1	391.2	0.4	−0.4	2.0	1.1	0.7
CAR	41° N, 104° W	0.6	0.8	1.3	1.0	1.5	1.7	−0.2	391.1	0.4	0.0	2.0	1.0	0.8
HIL	40° N, 88° W	0.5	0.7	1.1	1.1	1.3	1.8	−0.1	392.1	−0.4	−0.9	2.0	0.9	0.8
CMA	39° N, 74° W	0.3	0.5	1.4	0.9	1.5	1.8	−0.1	391.5	0.3	0.1	2.1	0.5	0.6
SGP	37° N, 98° W	0.4	0.5	1.1	0.8	1.2	1.7	0.0	391.4	0.0	−0.4	1.7	0.7	0.6
SCA	33° N, 79° W	0.2	0.4	1.1	0.5	1.2	1.8	−0.1	391.8	0.2	−0.8	1.6	0.3	0.5
AOA	29° N, 148° E	0.2	0.6	0.4	0.5	0.8	1.7	−0.1	392.4	0.0	0.0	1.4	0.5	0.6
TGC	28° N, 97° W	0.2	0.3	1.0	0.5	1.1	1.7	0.0	391.6	0.4	−0.3	1.9	0.5	0.4
RTA	21° S, 160° W	0.2	0.5	0.7	0.5	0.8	1.7	0.0	390.1	2.3	0.8	0.2	0.5	0.5
	Average land	0.5 ± 0.3	0.7 ± 0.4	1.2 ± 0.1	1.1 ± 0.4	1.4 ± 0.3	1.8 ± 0.0	0.0 ± 0.2	391.2 ± 0.6	0.6 ± 0.6	0.3 ± 0.9	2.0 ± 0.2	1.0 ± 0.2	0.8 ± 0.4
	Ave. land, corrected		0.6 ± 0.4		0.5 ± 0.0	1.3 ± 0.3					0.6 ± 0.6	0.3 ± 0.9	2.0 ± 0.2	0.9 ± 0.2	0.5 ± 0.4
AOA, RTA	Average ocean	0.2 ± 0.0	0.6 ± 0.1	0.6 ± 0.2	1.0 ± 0.4	0.8 ± 0.0	1.7 ± 0.0	−0.1 ± 0.1	391.3 ± 1.6	−1.2 ± 1.6	0.7 ± 0.1	0.8 ± 0.8	0.5 ± 0.0	0.6 ± 0.1
						(d) XCO_2 vs. ESRL aircraft								
PFA	66° N, 147° W	0.7	2.1	1.2	1.4	2.4	1.3	0.2	391.1	1.8	1.2	3.8	1.0	2.1
ETL	54° N, 105° W	0.7	1.3	1.5	1.9	2.0	0.9	0.0	390.3	0.7	0.6	2.8	2.1	1.4
ESP	49° N, 126° W	1.5	2.2	2.0	1.9	2.9	0.9	0.4	389.0	0.8	1.6	2.4	2.1	2.2
DND	47° N, 99° W	0.7	1.0	1.6	2.0	1.9	0.9	0.1	390.4	0.5	0.2	3.1	2.4	1.1
LEF	46° N, 90° W	0.9	1.1	1.5	1.7	1.8	1.0	0.0	391.4	0.1	−0.3	2.7	2.0	1.2
NHA	43° N, 71° W	0.7	0.9	1.7	1.5	1.9	1.0	−0.1	391.9	0.3	0.3	3.5	1.2	1.0
WBI	42° N, 91° W	0.9	0.8	1.4	1.0	1.6	0.8	−0.5	391.7	0.0	−0.3	2.3	0.8	0.9
THD	41° N, 124° W	1.1	1.2	1.7	1.1	2.1	0.9	0.4	390.3	0.7	1.6	2.2	1.0	1.3
BNE	41° N, 97° W	0.6	0.8	1.5	1.2	1.7	0.7	−0.4	391.7	−0.3	−0.8	2.2	1.3	0.9
CAR	41° N, 104° W	1.0	1.0	1.7	1.1	2.0	0.8	−0.6	391.5	−0.3	−0.7	2.1	1.2	1.1
HIL	40° N, 88° W	0.8	1.0	1.5	1.6	1.8	0.9	−0.3	393.1	−0.7	−1.3	2.4	1.3	1.0
CMA	39° N, 74° W	0.6	0.6	1.9	1.2	2.0	0.9	−0.2	392.3	0.0	0.0	2.8	0.8	0.8
SGP	37° N, 98° W	0.7	0.9	1.4	1.2	1.7	0.8	−0.1	392.1	−0.3	−0.5	1.9	1.1	1.0

Table B1. Continued.

Location	Latitude, longitude	Colocation error (ppm)	a corr. error (ppm)	b rand. error (ppm)	GOSAT prior bias (n=1) (ppm)	GOSAT error (n=1) (ppm)	Pred. error (n=1) (ppm)	Colocation bias (ppm)	True mean (ppm)	Prior bias (ppm)	GOSAT bias (ppm)	True stdev (n=1) (ppm)	Prior error (n=15) (ppm)	GOSAT error (n=15) (ppm)
SCA	33° N, 79° W	0.3	0.3	1.5	0.7	1.6	0.9	−0.2	392.7	0.2	−0.9	1.7	0.6	0.5
AOA	29° N, 148° E	0.2	0.5	0.6	0.5	0.8	0.6	−0.2	392.4	−1.2	0.3	1.4	0.5	0.6
TGC	28° N, 97° W	0.4	0.5	1.2	0.9	1.4	0.7	0.0	392.3	0.3	−0.3	1.9	0.9	0.6
RTA	21° S, 160° W	0.1	0.3	0.8	0.5	0.9	0.7	0.0	390.3	2.0	0.8	0.2	0.4	0.4
	Average land	0.8±0.3	1.0±0.5	1.6±0.2	1.5±0.4	1.9±0.4	0.9±0.1	−0.1±0.3	391.5±1.1	−0.3±0.6	−0.0±0.9	2.5±0.6	1.3±0.6	1.1±0.5
	Ave. land, corrected		0.7±0.5		0.5±0.0	1.7±0.4				−0.2±0.6	0.1±0.9		1.1±0.6	0.6±0.5
AOA, RTA	Average ocean	0.2±0.1	0.4±0.1	0.7±0.1	1.1±0.4	0.9±0.1	0.7±0.1	−0.1±0.1	391.4±1.5	0.4±2.3	0.6±0.4	0.8±0.8	0.5±0.1	0.5±0.1
(e) LMT GOSAT HIPPO ocean														
2° S	30–0° S	0.3	0.3	1.5	0.5	1.5	4.0	−0.1	390.9	2.0	−0.4	0.5	0.4	0.5
2° N	15–5° S	0.4	0.3	1.6	0.5	1.6	4.1	−0.1	390.7	2.2	−0.2	0.4	0.5	0.5
3° S	10° S–10° N	0.2	0.0	2.4	0.7	2.4	4.3	−0.4	393.5	−0.1	0.0	1.2	0.3	0.6
3° N	5° S–10° N	0.5	0.3	1.9	0.5	1.9	3.9	−0.4	393.4	−0.1	−0.4	0.6	0.4	0.6
4° S	10° N	0.1	0.5	1.5	0.5	1.6	4.6	−0.5	394.5	−3.0	0.2	0.3	0.4	0.6
4° N	15–30° N	0.3	0.4	1.5	1.2	1.5	4.2	−0.3	393.4	−4.2	−0.5	0.5	0.8	0.5
5° S	0–20° N	0.4	0.6	1.5	1.4	1.6	4.5	−0.2	390.7	−0.1	−0.4	0.6	1.0	0.7
5° N	10° S–20° N	0.5	0.5	1.3	1.1	1.4	4.5	−0.3	390.6	2.0	0.3	0.7	0.8	0.6
	Average	0.3±0.1	0.4±0.2	1.6±0.3	0.8±0.4	1.7±0.3	4.3±0.3	−0.3±0.2	392.2±1.6	−0.2±2.4	−0.2±0.3	0.6±0.3	0.6±0.3	0.6±0.6
(f) U GOSAT HIPPO ocean														
2° S	30–0° S	0.1	0.6	0.8	0.4	1.0	1.6	0.1	390.0	2.6	0.1	0.3	0.4	0.7
2° N	15–5° S	0.2	0.2	0.7	0.2	0.7	1.6	0.1	390.1	2.6	0.7	0.2	0.2	0.2
3° S	10° S–10° N	0.1	0.3	0.9	0.6	1.0	1.7	0.0	391.6	0.9	0.3	1.0	0.6	0.4
3° N	5° S–10° N	0.3	0.1	0.8	0.4	0.8	1.6	0.1	391.1	1.3	0.4	0.4	0.3	0.2
4° S	10° N	0.1	0.2	0.8	0.2	0.8	1.8	0.3	392.8	−0.2	0.2	0.2	0.2	0.3
4° N	15–30° N	0.1	0.2	0.7	0.3	0.7	1.6	−0.1	392.9	−0.3	0.2	0.2	0.2	0.3
5° S	0–20° N	0.1	0.3	0.8	0.3	0.9	1.8	0.1	390.4	1.2	−0.2	0.2	0.2	0.4
5° N	10° S–20° N	0.2	0.3	0.7	0.3	0.8	1.8	0.1	390.2	1.8	0.0	0.3	0.2	0.4
	Average	0.1±0.1	0.3±0.2	0.8±0.1	0.3±0.1	0.8±0.1	1.7±0.1	0.1±0.1	391.1±1.2	0.3±1.1	0.2±0.3	0.4±0.3	0.3±0.1	0.4±0.1
(g) XCO₂ GOSAT HIPPO ocean														
2° S	30–0° S	0.1	0.4	0.8	0.2	0.9	0.5	0.0	390.2	2.5	0.0	0.2	0.2	0.5
2° N	15–5° S	0.1	0.0	0.7	0.2	0.7	0.5	0.0	390.2	2.5	0.5	0.2	0.2	0.2
3° S	10° S–10° N	0.1	0.2	1.1	0.6	1.1	0.7	−0.1	392.0	0.6	0.2	1.1	0.5	0.3
3° N	5° S–10° N	0.3	0.0	0.9	0.4	0.9	0.5	0.0	391.6	1.0	0.2	0.5	0.2	0.2
4° S	10° N	0.1	0.3	0.9	0.2	0.9	0.8	0.1	393.2	−0.9	0.2	0.2	0.2	0.4
4° N	15–30° N	0.1	0.1	0.7	0.3	0.8	0.6	−0.1	393.1	−1.2	0.0	0.2	0.1	0.2
5° S	0–20° N	0.1	0.3	0.9	0.5	1.0	0.7	0.0	390.5	0.9	−0.2	0.3	0.3	0.4
5° N	10° S–20° N	0.2	0.3	0.8	0.5	0.8	0.8	0.0	390.3	1.8	0.0	0.3	0.3	0.4
	Average	0.1±0.2	0.2±0.2	0.9±0.1	0.4±0.2	0.9±0.1	0.6±0.1	0.0±0.1	391.4±1.3	0.9±1.4	0.1±0.2	0.4±0.3	0.3±0.1	0.3±0.1
(h) AJAX														
LMT		1.1			2.2	3.1	4.1	−0.6	393.6	−2.0	−0.2	2.8		
LMT, corrected*				1.9	2.9					−1.4	+0.4			
U		0.1			0.9	1.1	1.7	0.0	392.2	0.4	1.0	2.0		
XCO₂		0.2			0.6	0.9	0.8	−0.1	392.4	−0.1	0.7	2.4	−	−

* AJAX profiles are colocated within 1 h and 1° and therefore do not have multiple GOSAT matches to average.

References

Akagi, S. K., Yokelson, R. J., Wiedinmyer, C., Alvarado, M. J., Reid, J. S., Karl, T., Crounse, J. D., and Wennberg, P. O.: Emission factors for open and domestic biomass burning for use in atmospheric models, Atmos. Chem. Phys., 11, 4039–4072, doi:10.5194/acp-11-4039-2011, 2011.

Biraud, S. C., Torn, M. S., Smith, J. R., Sweeney, C., Riley, W. J., and Tans, P. P.: A multi-year record of airborne CO_2 observations in the US Southern Great Plains, Atmos. Meas. Tech., 6, 751–763, doi:10.5194/amt-6-751-2013, 2013.

Bowman, K. W., Rodgers, C. D., Kulawik, S. S., Worden, J., Sarkissian, E., Osterman, G., Steck, T., Lou, M., Eldering, A., Shephard, M., Worden, H., Lampel, M., Clough, S., Brown, P., Rinsland, C., Gunson, M., and Beer, R.: Tropospheric emission spectrometer: Retrieval method and error analysis, IEEE T. Geosci. Remote, 44, 1297–1307, 2006.

Chevallier, F., Ciais, P., Conway, T. J., Aalto, T., Anderson, B. E., Bousquet, P., Brunke, E. G., Ciattaglia, L., Esaki, Y., Frohlich, M., Gomez, A. J., Gomez-Pelaez, A. J., Haszpra, L., Krummel, P., Langenfelds, R., Leuenberger, M., Machida, T., Maignan, F., Matsueda, H., Morgui, J. A., Mukai, H., Nakazawa, T., Peylin, P., Ramonet, M., Rivier, L., Sawa, Y., Schmidt, M., Steele, P., Vay, S. A., Vermeulen, A. T., Wofsy, S., and Worthy, D.: CO_2 surface fluxes at grid point scale estimated from a global 21-year reanalysis of atmospheric measurements, J. Geophys. Res., 115, D21307, doi:10.1029/2010JD013887, 2010.

Chevallier, F., Palmer, P. I., Feng, L., Boesch, H., O'Dell, C. W., and Bousquet, P.: Toward robust and consistent regional CO_2 flux estimates from in situ and spaceborne measurements of atmospheric CO_2, Geophys. Res. Lett., 41, 1065–1070, doi:10.1002/2013GL058772, 2014.

Connor, B. J., Sherlock, V., Toon, G., Wunch, D., and Wennberg, P. O.: GFIT2: an experimental algorithm for vertical profile retrieval from near-IR spectra, Atmos. Meas. Tech., 9, 3513–3525, doi:10.5194/amt-9-3513-2016, 2016.

Connor, B. J., H. Boesch, G. Toon, B. Sen, C. Miller, and D. Crisp, Orbiting Carbon Observatory: Inverse method and prospective error analysis, J. Geophys. Res., 113, D05305, doi:10.1029/2006JD008336, 2008.

Conway, T. J., Tans, P. P., Waterman, L. S., Thoning, K. W., Kitzis, D. R., Masarie, K. A., and Zhang, N.: Evidence for interannual variability of the carbon cycle from the NOAA/CMDL global air sampling network, J. Geophys. Res., 99, 22831–22855, 1994.

Crisp, D., Fisher, B. M., O'Dell, C., Frankenberg, C., Basilio, R., Bösch, H., Brown, L. R., Castano, R., Connor, B., Deutscher, N. M., Eldering, A., Griffith, D., Gunson, M., Kuze, A., Mandrake, L., McDuffie, J., Messerschmidt, J., Miller, C. E., Morino, I., Natraj, V., Notholt, J., O'Brien, D. M., Oyafuso, F., Polonsky, I., Robinson, J., Salawitch, R., Sherlock, V., Smyth, M., Suto, H., Taylor, T. E., Thompson, D. R., Wennberg, P. O., Wunch, D., and Yung, Y. L.: The ACOS CO_2 retrieval algorithm – Part II: Global XCO_2 data characterization, Atmos. Meas. Tech., 5, 687–707, doi:10.5194/amt-5-687-2012, 2012.

Davies, D., Kumar, S., and Descloitres, J., Global fire monitoring using MODIS near-real-time satellite data, GIM International, 18, 41–43, 2004.

Deeter, M. N., Emmons, L. K., Francis, G. L., Edwards, D. P., Gille, J. C., Warner, J. X., Khattatov, B., Ziskin, D., Lamarque, J.-F., Ho, S.-P., Yudin, Attié, J.-L., Packman, D., Chen, J., Mao, D., and Drummond, J. R.: Operational carbon monoxide retrieval algorithm and selected results for the MOPITT instrument, J. Geophys. Res., 108, 4399, doi:10.1029/2002JD003186, 2003.

Deeter, M. N., Martínez-Alonso, S., Edwards, D. P., Emmons, L. K., Gille, J. C., Worden, H. M., Sweeney, C., Pittman, J. V., Daube, B. C., and Wofsy, S. C.: The MOPITT Version 6 product: algorithm enhancements and validation, Atmos. Meas. Tech., 7, 3623–3632, doi:10.5194/amt-7-3623-2014, 2014.

Deng, F., Jones, D. B. A., Walker, T. W., Keller, M., Bowman, K. W., Henze, D. K., Nassar, R., Kort, E. A., Wofsy, S. C., Walker, K. A., Bourassa, A. E., and Degenstein, D. A.: Sensitivity analysis of the potential impact of discrepancies in stratosphere-troposphere exchange on inferred sources and sinks of CO_2, Atmos. Chem. Phys., 15, 11773–11788, doi:10.5194/acp-15-11773-2015, 2015.

Denning, A. S., Collatz, G. J., Zhang, C., Randall, D. A., Berry, J. A., Sellers, P. J., Colello, G. D., and Dazlich, D. A.: Simulations of terrestrial carbon metabolism and atmospheric CO_2 in a general circulation model, Part 2: simulated CO_2 concentrations, Tellus, 48B, 543–567, 1996.

Dohe, S.: Measurements of atmospheric CO_2 columns using ground-based FTIR spectra, Doctor of Science dissertation, Karlsruhe Institute for Technology, Karlsruhe, Germany, 2013.

Feng, L., Palmer, P. I., Parker, R. J., Deutscher, N. M., Feist, D. G., Kivi, R., Morino, I., and Sussmann, R.: Estimates of European uptake of CO_2 inferred from GOSAT XCO2 retrievals: sensitivity to measurement bias inside and outside Europe, Atmos. Chem. Phys., 16, 1289–1302, doi:10.5194/acp-16-1289-2016, 2016.

Frankenberg, C., Kulawik, S. S., Wofsy, S. C., Chevallier, F., Daube, B., Kort, E. A., O'Dell, C., Olsen, E. T., and Osterman, G.: Using airborne HIAPER Pole-to-Pole Observations (HIPPO) to evaluate model and remote sensing estimates of atmospheric carbon dioxide, Atmos. Chem. Phys., 16, 7867–7878, doi:10.5194/acp-16-7867-2016, 2016.

Giglio, L., Descloitres, J., Justice, C. O., and Kaufman, Y. J.: An enhanced contextual fire detection algorithm for MODIS, Remote Sens. Environ., 87, 273–282, 2003.

GLOBALVIEW-CO2: Cooperative Global Atmospheric Data Integration Project, updated annually. Multi-laboratory compilation of atmospheric carbon dioxide data for the period 2000–2012 (obspack_co2_1_PROTOTYPE_v1.0.4b_2014-02-13), Compiled by NOAA Global Monitoring Division: Boulder, Colorado, USA, doi:10.3334/OBSPACK/1001, 2013.

Guerlet, S., Butz, A., Schepers, D., Basu, S., Hasekamp, O. P., Kuze, A., Yokota, T., Blavier, J.-F., Deutscher, N. M., Griffith, D. W. T., Hase, F., Kyro, E., Morino, I., Sherlock, V., Sussmann, R., Galli, A., Aben, I.: Impact of aerosol and thin cirrus on retrieving and validating X_{CO_2} from GOSAT shortwave infrared measurements, J. Geophys. Res.-Atmos., 118, 4887–4905, doi:10.1002/jgrd.50332, 2013.

Gurney, K. R., Law, R. M., Denning, A. S., Rayner, P. J., Baker, D., Bousquet, P., Bruhwiler, L., Chen, Y.-H., Ciais, P., Fan, S., Fung, I. Y., Gloor, M., Heimann, M., Higuchi, K., John, J., Maki, T., Maksyutov, S., Masarie, K., Peylin, P., Prather, M., Pak, B. C., Randerson, J., Sarmiento, J., Taguchi, S., Takahashi, T., and Yuen, C.-W.: Towards robust regional estimates of CO_2 sources and sinks using atmospheric transport models, Nature, 415, 626–630, 2002.

Hamill, P., Iraci, L., Yates, E., Gore, W., Bui, T. P., Tanaka, T., and Loewenstein, M.: A new instrumented airborne platform for atmospheric research, B. Am. Meteorol. Soc., 97, 397–404, doi:10.1175/BAMS-D-14-00241.1, 2016.

Houweling, S., Baker, D., Basu, S., Boesch, H., Butz, A., Chevallier, F., Deng, F., Dlugokencky, E. J., Feng, L., Ganshin, A., Hasekamp, O., Jones, D., Maksyutov, S., Marsha, J., Oda, T., O'Dell, C. W., Oshchepkov, S., Palmer, P. I., Peylin, P., Poussi, Z., Reum, F., Takagi, H., Yoshida, Y., and Zhuravlev, R.: An intercomparison of inverse models for estimating sources and sinks of CO_2 using GOSAT measurements, J. Geophys. Res.-Atmos., 120, 5253–5266, 2015.

Inoue, M., Morino, I., Uchino, O., Miyamoto, Y., Yoshida, Y., Yokota, T., Machida, T., Sawa, Y., Matsueda, H., Sweeney, C., Tans, P. P., Andrews, A. E., Biraud, S. C., Tanaka, T., Kawakami, S., and Patra, P. K.: Validation of XCO2 derived from SWIR spectra of GOSAT TANSO-FTS with aircraft measurement data, Atmos. Chem. Phys., 13, 9771–9788, doi:10.5194/acp-13-9771-2013, 2013.

Karion, A., Sweeney, C., Tans, P., and Newberger, T.: AirCore: An innovative atmospheric sampling system, J. Atmos. Ocean. Technol., 27, 1839–1853, doi:10.1175/2010JTECHA1448.1, 2010.

Kuai L., Wunch, D., Shia, R.-L., Connor, B., Miller, C., and Yung, Y.: Vertically constrained CO_2 retrievals from TCCON measurements, J. Quant. Spectrosc. Ra., 113, 1753–1761, 2012.

Kulawik, S. S., Osterman, G., Jones, D. B. A., and Bowman, K. W.: Calculation of altitude-dependent Tikhonov constraints for TES nadir retrievals, IEEE T. Geosci. Remote, 44, 1334–1342, 2006.

Kulawik, S., Wunch, D., O'Dell, C., Frankenberg, C., Reuter, M., Oda, T., Chevallier, F., Sherlock, V., Buchwitz, M., Osterman, G., Miller, C. E., Wennberg, P. O., Griffith, D., Morino, I., Dubey, M. K., Deutscher, N. M., Notholt, J., Hase, F., Warneke, T., Sussmann, R., Robinson, J., Strong, K., Schneider, M., De Mazière, M., Shiomi, K., Feist, D. G., Iraci, L. T., and Wolf, J.: Consistent evaluation of ACOS-GOSAT, BESD-SCIAMACHY, CarbonTracker, and MACC through comparisons to TCCON, Atmos. Meas. Tech., 9, 683–709, doi:10.5194/amt-9-683-2016, 2016.

Kuze, A., Suto, H., Shiomi, K., Kawakami, S., Tanaka, M., Ueda, Y., Deguchi, A., Yoshida, J., Yamamoto, Y., Kataoka, F., Taylor, T. E., and Buijs, H. L.: Update on GOSAT TANSO-FTS performance, operations, and data products after more than 6 years in space, Atmos. Meas. Tech., 9, 2445–2461, doi:10.5194/amt-9-2445-2016, 2016.

Lauvaux, T. and Davis, K. J.: Planetary boundary layer errors in mesoscale inversions of column-integrated CO2 measurements, J. Geophys. Res.-Atmos., 119, 490–508, doi:10.1002/2013jd020175, 2014.

Liu, J., Fung, I., Kalnay, E., and Kang, J. S.: CO transport uncertainties from the uncertainties in meteorological fields, Geophys. Res. Lett., 38, L12808, doi:10.1029/2011GL047213, 2011.

Liu, J., Bowman, K. W., and Henze, D. K.: Source-receptor relationships of column-average CO_2 and implications for the impact of observations on flux inversions, J. Geophys. Res.-Atmos., 120, 5214–5236, 2015.

Membrive, O., Crevoisier, C., Sweeney, C., Danis, F., Hertzog, A., Engel, A., Bönisch, H., and Picon, L.: AirCore-HR: A high resolution column sampling to enhance the vertical description of CH_4 and CO_2, Atmos. Meas. Tech. Discuss., doi:10.5194/amt-2016-236, in review, 2016.

Nehrkorn, T., Eluszkiewicz, J., Wofsy, S. C., Lin, J. C., Gerbig, C., Longo, M., and Freitas, S.: Coupled Weather Research and Forecasting-Stochastic-Time-Inverted Lagrangian Transport Model, Meteorol. Atmos. Phys., 107, 51–64, 2010.

O'Brien, D. M. and Rayner, P. J.: Global observations of the carbon budget, 2, CO_2 concentrations from differential absorption of reflected sunlight in the 1.61 µm band of CO_2, J. Geophys. Res., 107, 4354, doi:10.1029/2001JD000617, 2002.

O'Dell, C. W., Connor, B., Bösch, H., O'Brien, D., Frankenberg, C., Castano, R., Christi, M., Eldering, D., Fisher, B., Gunson, M., McDuffie, J., Miller, C. E., Natraj, V., Oyafuso, F., Polonsky, I., Smyth, M., Taylor, T., Toon, G. C., Wennberg, P. O., and Wunch, D.: The ACOS CO_2 retrieval algorithm – Part 1: Description and validation against synthetic observations, Atmos. Meas. Tech., 5, 99–121, doi:10.5194/amt-5-99-2012, 2012.

Peters, W., Jacobson, A. R., Sweeney, C., Andrews, A. E., Conway, T. J., Masarie, K., Miller, J. B., Bruhwiler, L. M. P., Petron, G., Hirsch, A. I., Worthy, D. E. J., van der Werf, G. R., Randerson, J. T., Wennberg, P. O., Krol, M. C., and Tans, P. P.: An atmospheric perspective on North American carbon dioxide exchange: CarbonTracker, P. Natl. Acad. Sci. USA, 104, 18925–18930, doi:10.1073/pnas.0708986104, 2007.

Prather, M. J., Zhua, X., Strahan, S. E., Steenrod, S. D., and Rodriguez, J. M.: Quantifying errors in trace species transport modeling, P. Natl. Acad. Sci. USA, 105, 19617–19621, doi:10.1073/pnas.0806541106,Dec 16, 2008

Rayner, P. J. and O'Brien, D. M.: The utility of remotely sensed CO_2 concentration data in surface source inversions, Geophys. Res. Lett., 28, 2429–2429, doi:10.1029/2001GL013115, 2001.

Rodgers, C. D.: Inverse methods for atmospheric sounding: theory and practice, London, WorldScientific, 2000.

Rubin, D. B.: The Bayesian Bootstrap, Ann. Stat., 9, 130–134, doi:10.1214/aos/1176345338, 1981.

Steck, T. and von Clarmann, T.: Constrained profile retrieval applied to the observation mode of the Michelson Interferometer for Passive Atmospheric Sounding, Appl. Opt., 40, 3559–3571, 2001.

Stephens, B. B., Gurney, K. R., Tans, P. P., Sweeney, C., Peters, W., Bruhwiler, L., Ciais, P., Ramonet, M., Bousquet, P., Nakazawa, T., Aoki, S., Machida, T., Inoue, G., Vinnichenko, N., Lloyd, J., Jordan, A., Heimann, M., Shibistova, O., Langenfelds, R. L., Steele, L. P., Francey, R. J., and Denning, A. S.: Weak northern and strong tropical land carbon uptake from vertical profiles of atmospheric CO_2, Science, 316, 1732–1735, 2007.

Sweeney, C., Karion, A., Wolter, S., Newberger, T., Guenther, D., Higgs, J. A., Andrews, A. E., Lang, P. M., Neff, D., Dlugokencky, E., Miller, J. B., Montzka, S. A., Miller, B. R., Masarie, K. A., Biraud, S. C., Novelli, P. C., Crotwell, M., Crotwell, A. M., Thoning, K., and Tans, P. P.: Seasonal climatology of CO_2 across North America from aircraft measurements in the NOAA/ESRL Global Greenhouse Gas Reference Network, J. Geophys. Res.-Atmos., 120, 5155–5190, doi:10.1002/2014jd022591, 2015.

Tanaka, T., Yates, E., Iraci, L., Johnson, M., Gore, W., Tadic, J., Loewenstein, M., Kuze, A., Frankenberg, C., Butz, A., and Yoshida, Y.: Two years comparison of airborne measurements of CO_2 and CH_4 with GOSAT at Railroad Valley, Nevada, IEEE T. Geosci. Remote, 54, 4367–4375, doi:10.1109/TGRS.2016.2539973, 2015.

Thoning, K. W., Tans, P. P., and Komhyr, W. D.: Atmospheric Carbon Dioxide at Mauna Loa Observatory 2. Analysis of the NOAA GMCC Data, 1974–1985, J. Geophys. Res., 94, 8549–8565, doi:10.1029/JD094iD06p08549, 1989.

Tikhonov, A.: On the solution of incorrectly stated problems and a method of regularization, Dokl. Acad. Nauk SSSR, 151, 501–504, 1963.

Twomey, S.: On the Numerical Solution of Fredholm Integral Equations of the First Kind by the Inversion of the Linear System Produced by Quadrature, Journal of the Association for Computing Machinery, 1701, 97–101, 1963.

von Clarmann, T., Glatthor, N., Grabowski, U., Hopfner, M., Kellmann, S., Kiefer, M., Linden, A., Mengistu Tsidu, G., Milz, M., Steck, T., Stiller, G. P., Wang, D. Y., Fischer, H., Funke, B., Gil-Lopez, S., and Lopez-Puertas, M.: Retrieval of temperature and tangent altitude pointing from limb emission spectra recorded from space by the Michelson Interferometer for Passive Atmospheric Sounding (MIPAS), J. Geophys. Res., 108, 4736, doi:10.1029/2003JD003602, 2003.

Wennberg, P. O., Roehl, C., Wunch, D., Toon, G. C., Blavier, J.-F., Washenfelder, R., Keppel-Aleks, G., Allen, N., Ayers, J.: TCCON data from Park Falls, Wisconsin, USA, Release GGG2014R0, TCCON data archive, hosted by the Carbon Dioxide Information Analysis Center, Oak Ridge National Laboratory, Oak Ridge, Tennessee, USA, doi:10.14291/tccon.ggg2014.parkfalls01.R0/1149161, 2014a.

Wennberg, P. O., Wunch, D., Roehl, C., Blavier, J.-F., Toon, G. C., Allen, N., Dowell, P., Teske, K., Martin, C., and Martin, J.: TCCON data from Lamont, Oklahoma, USA, Release GGG2014R0, TCCON data archive, hosted by the Carbon Dioxide Information Analysis Center, Oak Ridge National Laboratory, Oak Ridge, Tennessee, USA, doi:10.14291/tccon.ggg2014.lamont01.R0/1149159, 2014b.

Worden, H. M., Deeter, M. N., Edwards, D. P., Gille, J. C., Drummond, J. R., and Nédélec, P.: Observations of near-surface carbon monoxide from space using MOPITT multispectral retrievals, J. Geophys. Res.-Atmos., 115, 1831–18314, 2010.

Worden, J., Kulawik, S. S., Shephard, M. W., Clough, S. A., Worden, H., Bowman, K., and Goldman, A.: Predicted errors of tropospheric emission spectrometer nadir retrievals from spectral window selection, J. Geophys. Res.-Atmos., 109, D09308, doi:10.1029/2004JD004522, 2004.

Wunch, D., Toon, G. C., Blavier, J.-F. L., Washenfelder, R. A., Notholt, J., Connor, B. J., Griffith, D. W. T., Sherlock, V., and Wennberg, P. O.: The Total Carbon Column Observing Network, Philos. T. R. Soc. A, 369, 2087–2112, doi:10.1098/rsta.2010.0240, 2011a.

Wunch, D., Wennberg, P. O., Toon, G. C., Connor, B. J., Fisher, B., Osterman, G. B., Frankenberg, C., Mandrake, L., O'Dell, C., Ahonen, P., Biraud, S. C., Castano, R., Cressie, N., Crisp, D., Deutscher, N. M., Eldering, A., Fisher, M. L., Griffith, D. W. T., Gunson, M., Heikkinen, P., Keppel-Aleks, G., Kyrö, E., Lindenmaier, R., Macatangay, R., Mendonca, J., Messerschmidt, J., Miller, C. E., Morino, I., Notholt, J., Oyafuso, F. A., Rettinger, M., Robinson, J., Roehl, C. M., Salawitch, R. J., Sherlock, V., Strong, K., Sussmann, R., Tanaka, T., Thompson, D. R., Uchino, O., Warneke, T., and Wofsy, S. C.: A method for evaluating bias in global measurements of CO_2 total columns from space, Atmos. Chem. Phys., 11, 12317–12337, doi:10.5194/acp-11-12317-2011, 2011b.

Yokota, T., Yoshida, Y., Eguchi, N., Ota, Y., Tanaka, T., Watanabe, H., and Maksyutov, S.: Global Concentrations of CO_2 and CH4 Retrieved from GOSAT: First Preliminary Results, Sola, 5, 160–163, 2009.